



HAL
open science

The Coma Cluster at LOFAR Frequencies. II. The Halo, Relic, and a New Accretion Relic

A. Bonafede, G. Brunetti, L. Rudnick, F. Vazza, H. Bourdin, G. Giovannini, T.W. Shimwell, X. Zhang, P. Mazzotta, A. Simionescu, et al.

► **To cite this version:**

A. Bonafede, G. Brunetti, L. Rudnick, F. Vazza, H. Bourdin, et al.. The Coma Cluster at LOFAR Frequencies. II. The Halo, Relic, and a New Accretion Relic. *Astrophys.J.*, 2022, 933 (2), pp.218. 10.3847/1538-4357/ac721d . hal-03615544

HAL Id: hal-03615544

<https://hal.science/hal-03615544>

Submitted on 9 Mar 2023

HAL is a multi-disciplinary open access archive for the deposit and dissemination of scientific research documents, whether they are published or not. The documents may come from teaching and research institutions in France or abroad, or from public or private research centers.

L'archive ouverte pluridisciplinaire **HAL**, est destinée au dépôt et à la diffusion de documents scientifiques de niveau recherche, publiés ou non, émanant des établissements d'enseignement et de recherche français ou étrangers, des laboratoires publics ou privés.



The Coma Cluster at LOFAR Frequencies. II. The Halo, Relic, and a New Accretion Relic

A. Bonafede^{1,2,3} , G. Brunetti², L. Rudnick⁴ , F. Vazza^{1,2,3}, H. Bourdin^{5,6}, G. Giovannini^{1,2} , T. W. Shimwell^{7,8} , X. Zhang^{8,9}, P. Mazzotta^{5,6}, A. Simionescu^{8,9,10} , N. Biava^{1,2}, E. Bonnassieux^{1,2}, M. Brienza^{1,2}, M. Brüggén³ , K. Rajpurohit^{1,2,11} , C. J. Riseley^{1,2,12}, C. Stuardi^{1,2} , L. Feretti² , C. Tasse^{13,14}, A. Botteon⁸ , E. Carretti² , R. Cassano² , V. Cuciti³, F. de Gasperin^{2,3} , F. Gastaldello¹⁵ , M. Rossetti¹⁵, H. J. A. Rottgering⁸, T. Venturi², and R. J. van Weeren⁸

¹DIFA—Università di Bologna, via Gobetti 93/2, I-40129 Bologna, Italy; annalisa.bonafede@unibo.it

²INAF—IRA, Via Gobetti 101, I-40129 Bologna, Italy; IRA—INAF, via P. Gobetti 101, I-40129 Bologna, Italy

³Universität Hamburg, Hamburger Sternwarte, Gojenbergsweg 112, D-21029, Hamburg, Germany

⁴Minnesota Institute for Astrophysics, School of Physics and Astronomy, University of Minnesota, Minneapolis, MN 55455, USA

⁵Università di Roma Tor Vergata, Via della Ricerca Scientifica, I-00133 Roma, Italy

⁶INFN, Sezione di Roma 2, Università di Roma Tor Vergata, Via della Ricerca Scientifica, 1, Roma, Italy

⁷ASTRON, Netherlands Institute for Radio Astronomy, Oude Hoogeveensedijk 4, 7991 PD, Dwingeloo, The Netherlands

⁸Leiden Observatory, Leiden University, PO Box 9513, 2300 RA Leiden, The Netherlands

⁹SRON Netherlands Institute for Space Research, Niels Bohrweg 4, 2333 CA Leiden, The Netherlands

¹⁰Kavli Institute for the Physics and Mathematics of the Universe (WPI), The University of Tokyo, Kashiwa, Chiba 277-8583, Japan

¹¹Thüringer Landessternwarte, Sternwarte 5, D-07778 Tautenburg, Germany

¹²CSIRO Space & Astronomy, PO Box 1130, Bentley, WA 6102, Australia

¹³GEPI and USN, Observatoire de Paris, Université PSL, CNRS, 5 Place Jules Janssen, F-92190 Meudon, France

¹⁴Department of Physics and Electronics, Rhodes University, PO Box 94, Grahamstown, 6140, South Africa

¹⁵INAF—IASF Milano, via A. Corti 12, I-20133 Milano, Italy

Received 2022 March 2; revised 2022 May 16; accepted 2022 May 17; published 2022 July 15

Abstract

We present LOw Frequency ARray observations of the Coma Cluster field at 144 MHz. The cluster hosts one of the most famous radio halos, a relic, and a low surface brightness bridge. We detect new features that allow us to make a step forward in the understanding of particle acceleration in clusters. The radio halo extends for more than 2 Mpc, which is the largest extent ever reported. To the northeast of the cluster, beyond the Coma virial radius, we discover an arc-like radio source that could trace particles accelerated by an accretion shock. To the west of the halo, coincident with a shock detected in the X-rays, we confirm the presence of a radio front, with different spectral properties with respect to the rest of the halo. We detect a radial steepening of the radio halo spectral index between 144 and 342 MHz, at $\sim 30'$ from the cluster center, that may indicate a non-constant re-acceleration time throughout the volume. We also detect a mild steepening of the spectral index toward the cluster center. For the first time, a radial change in the slope of the radio–X-ray correlation is found, and we show that such a change could indicate an increasing fraction of cosmic-ray versus thermal energy density in the cluster outskirts. Finally, we investigate the origin of the emission between the relic and the source NGC 4789, and we argue that NGC 4789 could have crossed the shock originating the radio emission visible between its tail and the relic.

Unified Astronomy Thesaurus concepts: [Galaxy clusters \(584\)](#); [Non-thermal radiation sources \(1119\)](#); [Extragalactic radio sources \(508\)](#); [Intracluster medium \(858\)](#)

1. Introduction

Diffuse, non-thermal emission has been observed in more than 100 clusters of galaxies, revealing the existence of magnetic fields and relativistic particles on scales as large as a few megaparsecs. In the past decade, the advent of low-frequency, sensitive radio observations has brought about a major advance in the discovery of these objects and the characterization of their properties.

Synchrotron emission from the intracluster medium (ICM) has been observed in the form of giant radio halos, mini halos, and radio relics, depending on their location and morphology. Giant radio halos are found at the centers of merging galaxy clusters, co-spatial with the X-ray emitting gas, and with sizes of 1–2 Mpc. Mini halos only have sizes of a few hundred

kiloparsecs and are found mostly in cool-core clusters. Finally, radio relics are arc-like sources located in cluster outskirts, where they trace merger shock waves. We refer to van Weeren et al. (2019) for a recent review.

Since their discovery, it has been proposed that radio halos and relics are generated by shocks and turbulence driven in the ICM by cluster mergers (see, e.g., Brunetti & Jones 2014 for a review, and references therein). Although the details of the proposed mechanisms are not understood yet, radio halos have preferentially been found in merging clusters, supporting a connection between mergers and radio emission (Cuciti et al. 2015), and radio relics are often coincident with gas discontinuities detected in the X-ray and Sunyaev–Zel’dovich (SZ) images (e.g., Ogrea et al. 2013; Planck Collaboration et al. 2013). The origin of mini halos is still debated. They could originate either from turbulent motions that develop in the cluster core (e.g., ZuHone et al. 2013) or from hadronic collisions between cosmic-ray protons and thermal protons (e.g., Pfrommer & EnBlin 2004).

In the past years, the picture has become more complicated, and it has been found that some clusters with mini halos also host a larger-scale radio component, resembling a dimmer version of the giant radio halos but in non-merging objects (e.g., Savini et al. 2019; Raja et al. 2020). Moreover, a giant halo has also been found in a strong cool-core cluster, CL 1821+643 (Bonafede et al. 2014). In addition, relics and halos are sometimes connected through low-brightness radio bridges (van Weeren et al. 2012; Bonafede et al. 2021) that could be powered by mechanisms similar to those that are currently used to explain radio halos. On even larger scales, giant bridges of radio emission have been discovered, connecting massive clusters in a pre-merging state (e.g., Govoni et al. 2019; Botteon et al. 2020b).

Despite the differences between these types of sources, they all have a low surface brightness ($\sim 1 \mu\text{Jy arcsec}^{-2}$) at GHz frequencies. They also have steep radio spectra,¹⁶ with a spectral index $\alpha < -1$ that makes them brighter at low radio frequencies. Hence, the advent of deep, low-frequency radio surveys, such as the LOFAR Two-meter Sky Survey (LoTSS; Shimwell et al. 2017, 2019), has both increased the number of new detections (see, e.g., Biava et al. 2021; Riseley et al. 2022; Botteon et al. 2022; Hoang et al. 2022) and allowed the study of known objects with unprecedented sensitivity and detail.

The Coma cluster hosts the most famous and best studied radio halo, as well as a radio relic and a radio bridge connecting the two (see Figure 1). The emission from the Coma field has been the subject of many studies since its discovery (e.g., Large et al. 1959; Ballarati et al. 1981; Giovannini et al. 1991; Venturi et al. 1990; Kronberg et al. 2007; Brown & Rudnick 2011). In Paper I (Bonafede et al. 2021), we have analyzed the properties of the radio bridge and have shown under which conditions it can be powered by turbulent acceleration. In this paper, we focus on the radio halo and relic of the Coma cluster. New LOFAR data give us information in regions that have been so far inaccessible, providing important clues on the origin of the radio emission. Giovannini et al. (1993) first found that the spectrum of the halo between 326 MHz and 1.28 GHz is characterized by two different regions: a central one with $\alpha \sim -0.8$, and a peripheral one with $\alpha \sim -1.2$. The integrated spectrum, computed between 30 MHz and 4.8 GHz, shows a high-frequency steepening consistent with homogeneous in situ re-acceleration models. They also reported a smooth distribution of the radio surface brightness, with no evidence for substructures at the resolution of $\sim 50''$. Their results have been confirmed later on by several authors, such as Thierbach et al. (2003), who complemented the analysis with observations up to 4.8 GHz, where the halo is barely detected. The steepening of the halo at high frequencies has been subject to debate, as the decrement due to the SZ effect was initially not accounted for. After the observation of the SZ effect by the Planck satellite (Planck Collaboration et al. 2011, 2014), it has been possible to confirm the steepening of the radio emission (Brunetti et al. 2013). However, we note that data below 300 MHz, being taken in the 1980s, lack the sensitivity, resolution, calibration, and imaging accuracy that are allowed by present instruments and techniques. In particular, the observation at 151 MHz (Cordey 1985), i.e., the closest in frequency to LOFAR High Band Array (HBA), has a resolution of $\sim 70''$ and a sensitivity

of a few $\times 10 \text{ mJy beam}^{-1}$, which allowed the detection of the central part of the halo only. Similarly, observations at 43 and 73 MHz by Hanisch & Erickson (1980) did not allow us to properly subtract the emission from radio galaxies present in the cluster.

In addition to integrated spectral studies, better resolved spatial analysis of radio halos' spectral properties yields important information about the distribution of the component in the ICM (e.g., Rajpurohit et al. 2020, 2021a, 2021b). The halo in the Coma cluster offers a unique chance to perform spatially resolved studies of the halo brightness and of its connection between thermal and non-thermal plasma (e.g., Govoni et al. 2001; Brown & Rudnick 2011). So far, these studies have been inhibited by the lack of resolution, as it is often necessary to convolve the radio images with large Gaussian beams to recover the full halo emission.

LOFAR (van Haarlem et al. 2013), thanks to its sensitivity and resolution, provides a step forward for precise measurements of the halo size and flux density and for resolved studies. In this paper, we study the radio emission from the Coma cluster at 144 MHz, using data from LoTSS (Shimwell et al. 2019; Shimwell et al., in press) after ad hoc reprocessing. We also use published data and reprocessed archival X-ray and radio observations to perform a multiwavelength study of the emission.

This paper is organized as follows: In Section 2 we describe the observations and data reduction procedures. In Section 3 we present the main sources of diffuse emission, both known and newly discovered. The radio halo is analyzed in Section 4, its spectrum is analyzed in Section 5, and its correlation with the thermal gas is shown in Sections 6 and 7. In particular, in Sections 5.3 and 6.4, the halo properties, as discussed in the framework of turbulent re-acceleration models, and constraints to the model parameters are derived. In Section 8, we use cosmological MHD simulations to reproduce the thermal/non-thermal properties of the Coma cluster. In Section 9, the halo front is analyzed and its origin is discussed in connection with the shock wave found by X-ray and SZ studies. We also analyze the emission detected between the relic and the radio galaxy NGC 4789 in Section 10. Finally, results are discussed in Section 11. Throughout this paper, we use a Λ CDM cosmological model, with $\Omega_\Lambda = 0.714$, $H_0 = 69.6 \text{ km s}^{-1} \text{ Mpc}^{-1}$. At the Coma redshift ($z = 0.0231$) the angular to linear scale is $0.469 \text{ kpc arcsec}^{-1}$ and the luminosity distance $D_L = 101.3 \text{ Mpc}$.

2. Observations Used in This Work

2.1. LOFAR Data and Data Reduction

The data used in this work are part of the LoTSS (Shimwell et al. 2019, Shimwell et al. 2022) and consist of two pointings of 8 hr each taken with LOFAR (van Haarlem et al. 2013) HBA antennas, in the DUAL_INNER mode configuration. Each pointing is 8 hr long, bookended by 10-minute observations of a calibrator (3C 196), used to correct for the ionospheric Faraday rotation, clock offsets, instrumental XX and YY phase offsets, and time-independent amplitude solutions. The pointings are specified in Table 1, together with the distance from the central source NGC 4874, at the cluster center. Observations are centered at 144 MHz and have a 48 MHz total bandwidth. After preprocessing and direction-independent calibration, data are averaged into 24 visibility files, each

¹⁶ Throughout this paper, we define the spectral index α as $S(\nu) \propto \nu^\alpha$, where S is the flux density at the frequency ν .



Figure 1. Composite IR-radio image of the Coma cluster field. In white the IR image in bands 1, 2, and 3 of the Wide-field Infrared Survey Explorer is shown. The red-orange color scale shows the composite radio image of the diffuse emission at $1'$ for the diffuse emission and of $20''$ for the sources in the field.

Table 1
LOFAR Observations Details

LoTSS Pointing	R.A. (deg)	Decl. (deg)	Time (hr)	Dist. of NGC 4874 (deg)
P192+27	192.945	27.2272	8	1.88
P195+27	195.856	27.2426	8	1.11

having a bandwidth of 1.953 MHz with a frequency resolution of 97.6 kHz and a time resolution of 8 s. For details about preprocessing and direction-independent calibration steps, we refer to Shimwell et al. (2019), where LoTSS data acquisition and processing are both explained in detail. The direction-dependent calibration has been made using the LoTSS DR2 pipeline, but with a slightly different procedure to account for the large-scale emission present in the Coma field. Specifically, we have included all baselines in imaging and calibration, while the LoTSS DR2 pipeline applies an inner uv -cut of the visibilities below 100 m to eliminate radio frequency interferences on the shortest baselines and filter out large-scale Galactic emission that would make the process of calibration and imaging more difficult. The two pointings have been calibrated separately, and unrelated sources have been subtracted from the visibilities through a multistep procedure, for which we refer the reader to Bonafede et al. (2021). Briefly, we first subtracted all the sources outside a radius of 1.5°

centered on the cluster, using the model components obtained from an image at $20''$ resolution with no inner uv -cut, and using a threshold of 5σ ($0.75 \text{ mJy beam}^{-1}$). The subtracted data have been reimagined using a uv -cut of 300 m to filter out the diffuse emission from the ICM, and the model components have been subtracted using a threshold of $0.6 \text{ mJy beam}^{-1}$. Data have been reimagined again to check for the presence of residual emission from discrete sources using a uv -cut of 100 m. Residual emission associated with Active Galactic Nuclei (AGN) and sources unrelated to the halo and relic emission has been identified and subtracted by the data. The sources NGC 4789 and NGC 4839 have not been subtracted in order to study how their emission is connected to the relic and bridge, respectively. Two diffuse patches of emission to the west of Coma are still present and have been deconvolved in the imaging runs. They are discussed in the following sections.

The images used in this work have been done in a different way than in Bonafede et al. (2021), taking advantage of the new implementations that have been added to the imaging software in the past months. Imaging has been done with DDFacet (Tasse et al. 2018), using the recently added features that allow us to deconvolve large-scale emission in joint-deconvolution mode. We used the Sub Space Deconvolution (SSD) algorithm (Tasse et al. 2018 and references therein) to better model the clean components. Typically, four major cycles were needed to achieve a noise-like residual map. The

Table 2
Images Used in This Work

Image Name	Freq. (MHz)	Resolution	σ_{rms} (mJy beam $^{-1}$)	Figure
LOFAR as LoTSS 6	144	6" \times 6"	0.1	Figure 5
LOFAR as LoTSS 20	144	20" \times 20"	0.15	Figure 3
LOFAR 35"	144	35" \times 35"	0.2	Figure 3 (top panel), Figure 5
LOFAR 1'	144	60" \times 60"	0.4	Figure 2
WSRT H	342	134" \times 68"	0.4	Brown & Rudnick (2011)
LOFAR as WSRT H	144	134" \times 68"	1.5	Figure 20
WSRT R	326	150" \times 100"	1.2	Giovannini et al. (1991), Bonafede et al. (2021)
LOFAR as WSRT R	144	150" \times 100"	1	

beam correction has been applied in the image plane, interpolating the beams of the two different pointings in the direction of Coma. Different images have been produced, as listed in Table 2, at various resolutions to highlight the emission from discrete sources and from the diffuse emission. To align the flux scale to LoTSS, we have extracted the fluxes from the sources in the Coma field and followed the same bootstrap procedure described in Hardcastle et al. (2016), which is based on the NRAO VLA Sky Survey (NVSS; Condon et al. 1998).

2.2. XMM-Newton and ROSAT Data

We used the XMM-Newton Science Analysis System (SAS) v18.0.0 for data reduction. The ObsIDs we used are listed in the Appendix. Event files from the MOS and pn detectors were generated from the observation data files with the tasks `emproc` and `epproc`. The out-of-time (OoT) events of pn were corrected following the user guide.¹⁷ We used stacked Filter Wheel Closed (FWC) event files to generate non-X-ray-background (NXB) maps. For each ObsID, the FWC event files were reprojected using task `evproject` to match the observation. NXB maps were scaled to match the NXB level of each count image. For MOS, the scale factor was calculated using the ratio of out-of-field-of-view (OoFoV) count rates. For pn, even the OoFoV area can be contaminated by soft protons, and it cannot be used for an accurate rescaling of the NXB (Gastaldello et al. 2017; Zhang et al. 2020; Marelli et al. 2021). On the other hand, the pn instrumental background shows a similar long-term variability to that of Chandra’s ACIS-S3 chip; therefore, we used this information for rescaling the pn NXB level in the observations (details are provided in Zhang et al., in preparation).

The corresponding exposure maps were generated using the task `eexppmap` with parameter `withvignetting=yes`. Point sources were detected and filled by the tasks `wavdetect` and `dmfilth` in the Chandra Interactive Analysis of Observations (CIAO) v4.13 package. We stacked individual count maps, exposure maps, and NXB maps, respectively, using the 0.5–2.0 keV energy band. We divided the NXB-subtracted count image by the exposure map to generate the flux map. After removing the instrumental background and correcting for telescope vignetting, a constant sky background was further subtracted from the images. The level of this background was estimated from the median flux in an annulus spanning radii of 60'–70'. Note that Mirakhor & Walker (2020) do detect a signal from the Coma ICM even at these large radii, albeit in a narrower energy interval of 0.7–1.2 keV, where the

signal-to-background ratio is optimized. The sky background used here may therefore be slightly overestimated, but this does not have an impact on the radii of interest considered in our XMM-Newton analysis (limited in this case mostly within the cluster’s R_{500}).

We furthermore used the four archival observations of the Coma cluster performed in 1991 June by the ROSAT Position Sensitive Proportional Counter (PSPC). These pointings extend out to radii of 60'–70', totaling a clean exposure time of 78 ks. The data reduction was performed exactly as already described in Simionescu et al. (2013) and Bonafede et al. (2021). The low instrumental background of ROSAT makes these data an important complement to XMM-Newton in the faint cluster outskirts.

2.3. Planck Data

We used six Planck frequency maps acquired by the High Frequency Instrument (HFI) and the corresponding energy responses released in 2018 by the Planck collaboration (Planck Collaboration et al. 2020). The average frequencies of the HFI maps are 100, 143, 217, 353, 545, and 857 GHz. The nominal angular resolutions of the maps are 9'69, 7'30, 5'02, 4'94, 4'83, and 4'64, respectively. Following prescriptions of Galactic thermal dust studies performed by the Planck Collaboration (Planck Collaboration et al. 2014), we corrected HFI maps for individual offsets that maximize their spatial correlation with neutral hydrogen density column measurements performed in regions of the sky characterized by their low dust emissivity and by the exclusion of prominent SZ sources.

This multi-frequency data set allowed us to map the thermal SZ Compton parameter in a 4 deg² sky area centered on Coma, following the spectral imaging algorithm described in Baldi et al. (2019). Briefly, the Compton parameter, y , is jointly mapped in the wavelet space with the Cosmic Microwave Background anisotropies and with the Galactic thermal dust emissivity. This is achieved via a spatially weighted likelihood approach that includes the smoothing effect of individual HFI beams in the reconstruction of B3-spline wavelet coefficients. In order to best restore anisotropic details, a curvelet transform is eventually computed from these wavelet coefficients and denoised via a soft thresholding that we parameterize as a function of local values of the noise standard deviation. The resulting y -map has a resolution (FWHM of the point-spread function) of 5', i.e., a factor 2 higher than the one published in Planck Collaboration et al. (2013).

2.4. WSRT Data

We use data from the Westerbork Synthesis Radio Telescope (WSRT) at ~ 325 MHz. Part of these data come from the

¹⁷ http://xmm-tools.cosmos.esa.int/external/xmm_user_support/documentation/sas_usg/USG/removingOoTimg.html

Table 3
Source Properties at 144 MHz

Source Name	Dist.	LAS	$S_{144 \text{ MHz}}$	$P_{144 \text{ MHz}}$
Halo	...	71'–2.00 Mpc	Jy 12 ± 2	W/Hz $1.5 \pm 0.2 \times 10^{25}$
Accretion relic	2°1–3.55 Mpc	55'–1.5 Mpc	0.47 ± 0.07	$5.7 \pm 0.9 \times 10^{23}$
Relic	73'–2.0 Mpc	38'–1.1 Mpc	2.4 ± 0.4	$3.0 \pm 0.4 \times 10^{24}$
NAT–relic connection	79'–2.3 Mpc	10'–280 kpc	0.7 ± 0.1	$9 \pm 1 \times 10^{23}$

Note. Column (1): name of the diffuse source. Column (2): distance from the cluster center. Column (3): largest angular size measured above the $2\sigma_{\text{rms}}$ contour. Column (4): flux density measured above the $2\sigma_{\text{rms}}$ contour. Column (5): radio power at 144 MHz. The K -correction is applied assuming $\alpha = -1, -1, -1.2, \text{ and } -1.4$ for the halo, accretion relic, relic, and NAT–relic connection, respectively.

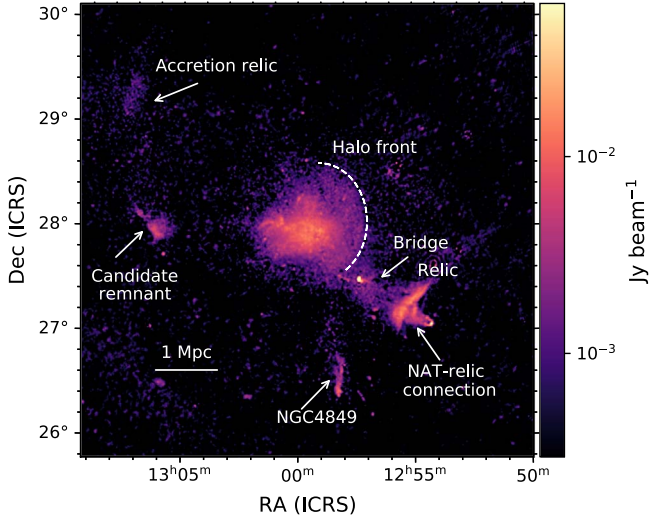


Figure 2. LOFAR emission of the Coma field at the resolution of 1'. The candidate accretion relic, halo front, bridge, relic, and NAT–relic connection are labeled.

observations published in Venturi et al. (1990) and Giovannini et al. (1991), which we have reimaged as explained in Bonafede et al. (2021). In this work, we also use more recent WSRT observations published by Brown & Rudnick (2011) that recover a larger fraction of the radio halo but are more affected by imaging and calibration artifacts due to the presence of the source Coma A, north of the relic. Brown & Rudnick (2011) observations are used here to study the spectral properties of the halo, while Venturi et al. (1990) and Giovannini et al. (1991) observations are used here to study the spectral index in the relic region. In Table 2, these images and their main properties are listed. We refer to the image published by Brown & Rudnick (2011) as WSRT H, as it is used to study the halo emission, and to the image published by Venturi et al. (1990) and Giovannini et al. (1991) as WSRT R, as it is used to study the relic region.

3. Components of the Diffuse Emission

The radio emission from the Coma field consists of several different components, either associated with the ICM or originating from the interaction of the radio galaxies with the environment. In Figure 2, the diffuse emission from the Coma cluster field is shown, after the subtraction of radio galaxies and point sources. The most relevant features are labeled. As already known, the Coma cluster hosts a radio halo, a radio relic, and a bridge of low surface brightness emission

connecting the two. In addition to these components, several new features are detected in our LOFAR observations. In this section, we present the emission from the diffuse sources as imaged by LOFAR at 144 MHz. An analysis of their properties that includes radio images at other frequencies and the comparison with the X-ray emission from the ICM is presented in the following sections for each source separately.

3.1. The Radio Halo

At 144 MHz, the radio halo appears larger than at higher frequencies, with a Largest Angular Scale (LAS) of 1°2, measured east to west, corresponding to ~ 2 Mpc (see Table 3). The halo appears to be composed of a central, bright core and a larger, weaker component that is asymmetrical and more pronounced toward the west (see Figure 3). The inner portion of the halo is what we define the “halo core.”¹⁸ This part of the halo is the one visible in the LoTSS images that impose an inner uv -cut of 80λ , corresponding to $\sim 43'$. The 20'' resolution of LoTSS, here reproduced using the same uv -range restriction, provides a detailed image of the inner portion of the halo. Clearly, the emission from the halo core is brighter than the rest, and its surface brightness is characterized by bright filaments of radio emission, marked with arrows in Figure 3. Despite being the best studied radio halo, this is the first time that features such as these filaments are detected in its diffuse emission.

Outside the halo core, low surface brightness emission is detected, which is brighter toward the west. We call this emission the “outer halo” and discuss in Sections 4 and 6 whether the halo core and the outer halo show different properties, as recently proposed for some cool-core clusters (Savini et al. 2018, 2019; Biava et al. 2021; Riseley et al. 2022). The emission from the outer halo is only visible when baselines shorter than 80λ are included in the image, and hence it is filtered out in the LoTSS images.

In the right panel of Figure 3, we show the halo in the LOFAR 35'' image, after the subtraction of the unrelated radio sources. To the west, the halo has a sharp edge coincident with the halo front (see Figure 2 for labeling) already found by Brown & Rudnick (2011) and coincident with the shock front detected in the X-rays (Simionescu et al. 2013) and SZ (Planck Collaboration et al. 2013). In Figure 4 we show the radio profile computed in annuli across the halo front in comparison with the rest of the cluster. The two sectors have azimuth angles from 47° to 287° (Coma) and from 323° to 48° (front, centered in R.A. = 12:59:07, decl. = +28:01:31). The south-west (SW) part of the halo, toward the radio bridge, has been

¹⁸ The halo core and outer halo are labeled in Figure 11.

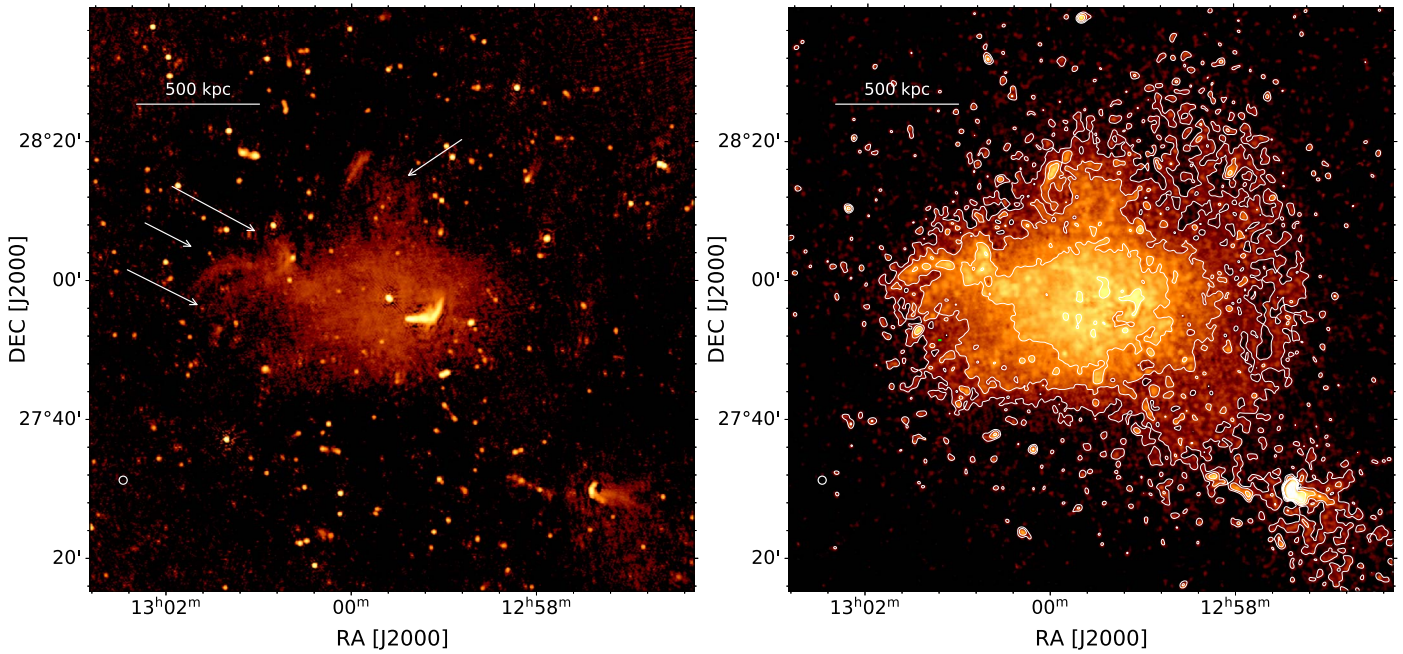


Figure 3. Left panel: zoom-in of the radio halo from the 20'' image, which is made imposing an inner uv -cut (image LOFAR as LoTSS 20 in Table 2). The halo core and the radio galaxies both of Coma and of the field are visible. The black bowl around the core indicates that large-scale diffuse emission is filtered out. White arrows mark the filaments (three arrows on the left) and the radio loop (arrow on the upper right). Right panel: same as the left panel, but from the 35'' image, where all the baselines have been included in the image and the discrete sources have been subtracted (see text for details). The outer halo and the halo front are well visible. Contours start at $3\sigma_{\text{rms}}$ and are spaced by a factor of 2.

excluded. While the average cluster profile shows a smooth radial decline, a sharp edge is visible around $\sim 1900''$ from the cluster center, coincident with the radio front found by Brown & Rudnick (2011).

Toward the SW, the spherical front continues and its brightness becomes weaker and merges with the emission from the radio bridge. The total flux density of the radio halo, measured from the images above $2\sigma_{\text{rms}}$, is 10 ± 2 Jy at 144 MHz. The main properties of the radio halo are listed in Table 3.

3.2. The Radio Relic and The NAT–Relic Connection

To the SW of the Coma cluster, a radio relic has been discovered by Ballarati et al. (1981) and studied by several authors afterward (Venturi et al. 1990; Giovannini et al. 1993; Brown & Rudnick 2011; Bonafede et al. 2013; Ogrea & Brüggner 2013). However, the presence of the bright source Coma A, at the northwest (NW) of the relic, has always made its study difficult. Residual calibration errors remain in the LOFAR image (see Figure 5) and make it difficult to determine whether the relic extension to the NW is real. We note that the same extension has also been detected by single-dish observations at 1.4 GHz, where it also appears polarized (Brown & Rudnick 2011). Despite this, because of its questionable nature, we adopt a conservative approach and do not include it in our discussion of the relic.

The radio relic has an LAS of $38'$, corresponding to ~ 1.1 Mpc at the Coma redshift. Its emission is connected on both sides to two head–tail radio galaxies, namely, NGC 4839 to the northeast (NE) and NGC 4789 to the SW of the relic. From NGC 4839, we detect diffuse emission that blends into the bridge and relic emission (Bonafede et al. 2021). The surface brightness of the relic is not uniform but composed of patchy and filamentary substructures (see Figure 5). Stripes of

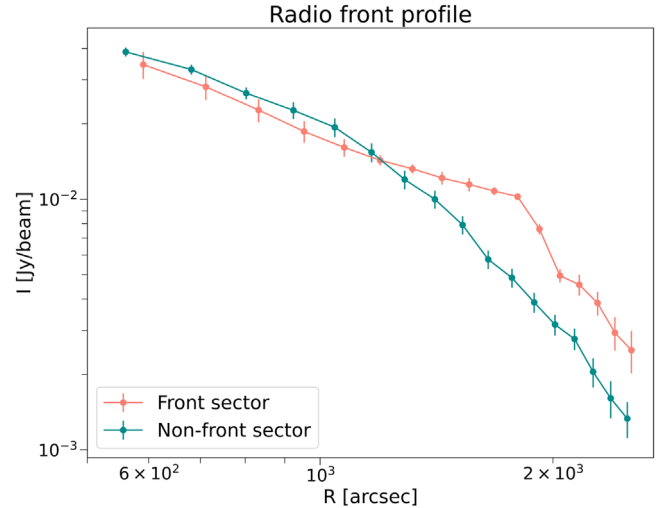


Figure 4. Radio profile of the Coma halo from the LOFAR image at 2'' resolution across the halo front in comparison with the rest of the halo. Error bars represent statistical errors only.

radio emission depart from the relic and are directed toward the bridge and NGC 4839. A similar stripe is detected also near the tail of NGC 4839, directed toward the relic. These features could be regions where the magnetic field has been amplified and/or where the plasma has been stripped from the tail of NGC 4789. The surface brightness of these stripes is a factor 2–3 higher than the nearby emission, and their size is $\sim 11/7$, which corresponds to 300 kpc at the Coma's redshift.

Beyond the relic, toward the SW, the narrow angle tail (NAT) galaxy NGC 4789 appears connected to the relic, as already found by, e.g., Giovannini et al. (1991). The connection between the relic and NGC 4789 has been interpreted as the tail of NGC 4789 feeding the relic with radio plasma

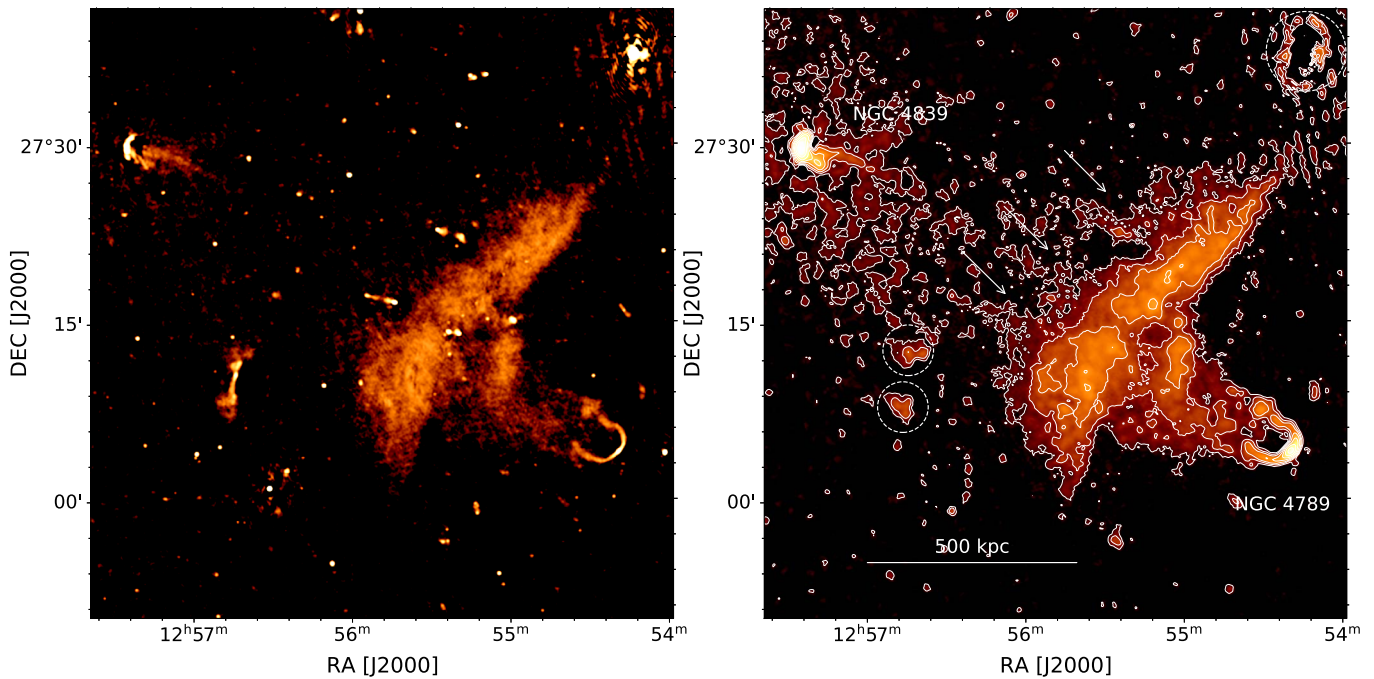


Figure 5. Zoom-in of the radio relic region. Left panel: 6'' image showing the complex emission that links the source NGC 4789 to the relic emission. Right panel: 35'' image. The source NGC 4789 is labeled. Arrows mark the position of the stripes that depart from the relic toward NGC 4839. White dashed circles indicate residuals from the subtraction of the lobes of NGC 4827, a Coma radio galaxy, and Coma A. Contours start at $3\sigma_{\text{rms}}$ and are spaced by a factor of 2.

(e.g., Enblin & Gopal-Krishna 2001). In Section 10, we will investigate the possible origin of this emission.

3.3. Diffuse Emission from NGC 4849

To the south of Coma, we detect diffuse emission, elongated in the north–south direction, with a size of $\sim 27'$. This emission seems associated with the radio galaxy NGC 4839, located at R.A. = $12^{\text{h}}58^{\text{m}}12^{\text{s}}.679$, decl. = $+26^{\circ}23'48''.77$, at redshift $z = 0.01966$. Its angular size translates into a linear size of ~ 650 kpc (see Figure 6). From the 6'' resolution image, the core of NGC 4849 is visible, and a hint of jet emission in the north–south direction is also present. A second bright component is located at the south of the core, which could be either an unrelated radio source seen in projection or the lobes of NGC 4849. The maximum extension of this tail in the WSRT image is $\sim 7'$. Using the WSRT H and “LOFAR as WSRT H” images (see Section 2 and Table 2) and taking into account the higher noise of the WSRT image in that region, we derive a 2σ limit for the spectral index of the tail $\alpha < -2$. Analyzing the emission of this source is not the aim of this paper; we note that similar steep spectrum tails have been found in the outskirts of other clusters (e.g., A1132, Wilber et al. 2018; A2255, Botteon et al. 2020a), likely tracing the motion of the galaxy in the ICM. The long tail of aged cosmic-ray electrons (CRE) left behind by these sources during their motion provides seed electrons that could be re-accelerated by turbulence and shocks.

3.4. Accretion Relic

After the subtraction of unrelated sources, two extended patches of diffuse emission are visible at the periphery of Coma, to its NE and east (see Figure 7). The diffuse component at the eastern side of Coma is not associated with any Coma cluster galaxy (Pizzo 2010). Pizzo (2010) also

noticed that this source lies at the crossroads of two filaments of galaxies, pointing toward the clusters A2197 and A2199, respectively, and suggested that this emission could be due to the accretion of matter toward the Coma cluster. Our images have a higher resolution and allow us to recognize a double-lobe structure that resembles a radio galaxy. However, no core is obviously associated with it in the 6'' and 20'' images (see Figure 7). We tentatively label this source as a “candidate remnant”, but we note that its classification remains uncertain. Indeed, given its large angular size ($\sim 27'$) and the lack of an optical identification at the Coma cluster redshift, it would have a very large linear size if it were in the background of Coma.

The other diffuse patch in the NE part of Coma is entirely new and has an arc-like morphology and a weak uniform brightness. This emission does not appear connected to any discrete source (see Figure 7). When convolving the image to a resolution of $2'$, it has a largest angular size of $\sim 55'$, which would correspond to 1.5 Mpc at the cluster redshift, and it is located at $\sim 2.1^\circ$ from the cluster center. At the Coma redshift, this distance corresponds to ~ 3.6 Mpc, while the cluster virial radius¹⁹ is ~ 2.9 Mpc. Since recent studies (e.g., Malavasi et al. 2020) have found an intergalactic filament of galaxies in the NW direction from the Coma cluster, this source could be connected to the cluster and its large-scale environment. Hence, we consider it plausible that this is an “accretion relic,” though more data supporting our hypothesis are needed. Considering that accretion shocks on these scales should be characterized by a strong Mach number ($\mathcal{M} \gg 5$; e.g., Hong et al. 2014), a strong prediction in this case would be that the radio spectrum of this emission should be $\alpha \propto \nu^{-1}$ and also characterized by a large degree of polarization. The properties of this accretion relic are listed in Table 3.

¹⁹ R_{100} is considered here to be a good approximation of the virial radius, as the cluster redshift is 0.023.

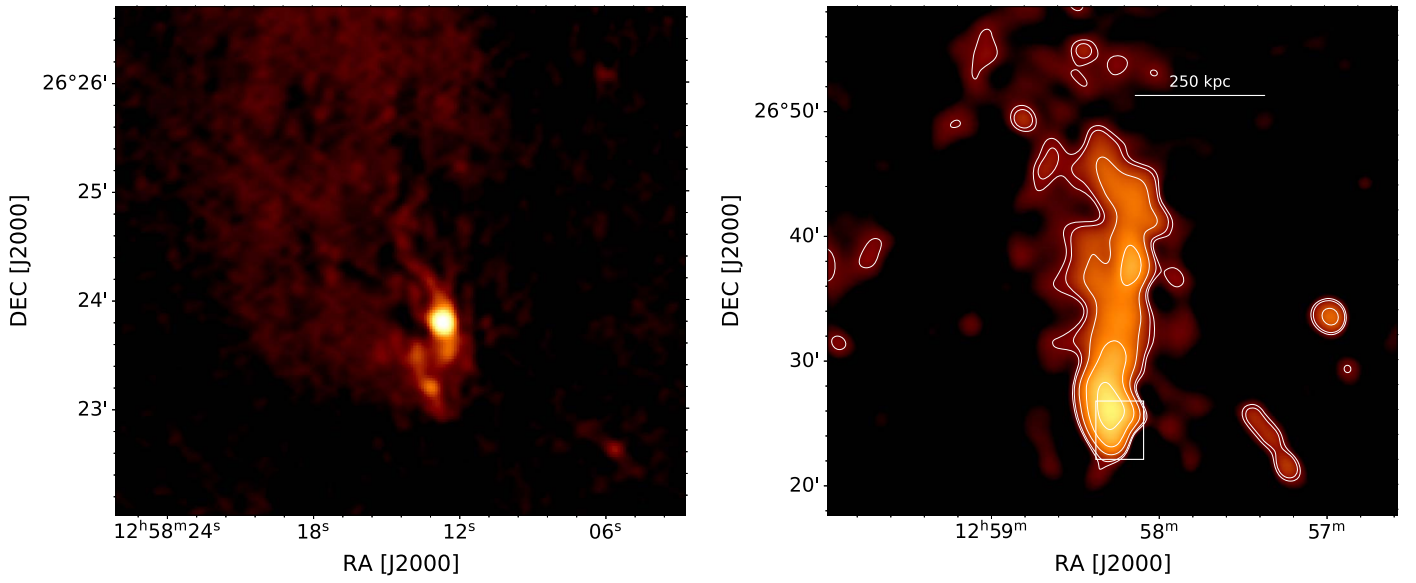


Figure 6. Zoom-in of the region of NGC 4849, to the south of Coma. Left panel: 6'' image from LoTSS showing the core of NGC 4849. Right panel: 1' image showing the full extent of the tail. The white box marks the region shown in the left panel. Contours start at 3σ and are spaced by a factor 2.

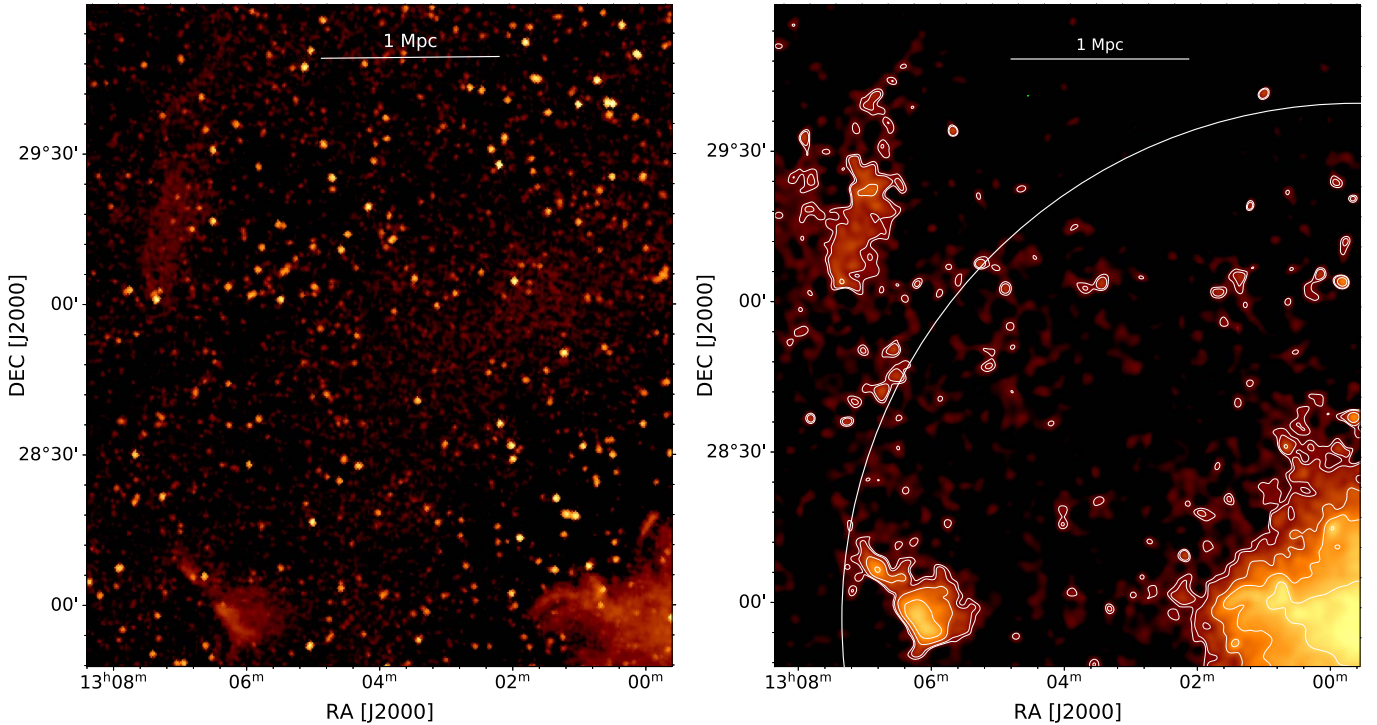


Figure 7. Zoom-in of the region of the accretion relic. Left panel: 20'' image from LoTSS showing the diffuse emission of the accretion relic (upper left), the candidate remnant source (lower left), and all the radio sources in the field. Right panel: same as the left panel, but from the 2' image. Contours are plotted at (3, 4, 8, 16, 32, 64) σ_{rms} . The white circle is centered on the Coma cluster centre and has a radius $r = R_{100}$.

4. The Radio Halo Profile

To characterize the halo properties, we have fitted its surface brightness profile adopting the approach first proposed by Murgia et al. (2009) and more recently generalized by Boxelaar et al. (2021) to account for asymmetric halo shapes. The main novelty of this procedure is that the profiles are fitted to a two-dimensional image directly, using MCMC to explore the parameter space, rather than to a radially averaged profile. In addition, the fitting procedure by Boxelaar et al. (2021) allows one to fit also elliptical and skewed (asymmetric) models. We

refer to Boxelaar et al. (2021) for a detailed explanation and summarize here the relevant parameters. The surface brightness model is given by

$$I(r) = I_0 \exp^{-G(r)}, \quad (1)$$

where I_0 is the central surface brightness and $G(r)$ a radial function. $G(r) = \left(\frac{1r^2}{r_e^2}\right)^{0.5}$ for the circular model, while $G(r) = \left(\frac{x^2}{r_1^2} + \frac{y^2}{r_2^2}\right)^{0.5}$ for the elliptical models, where r_e is the

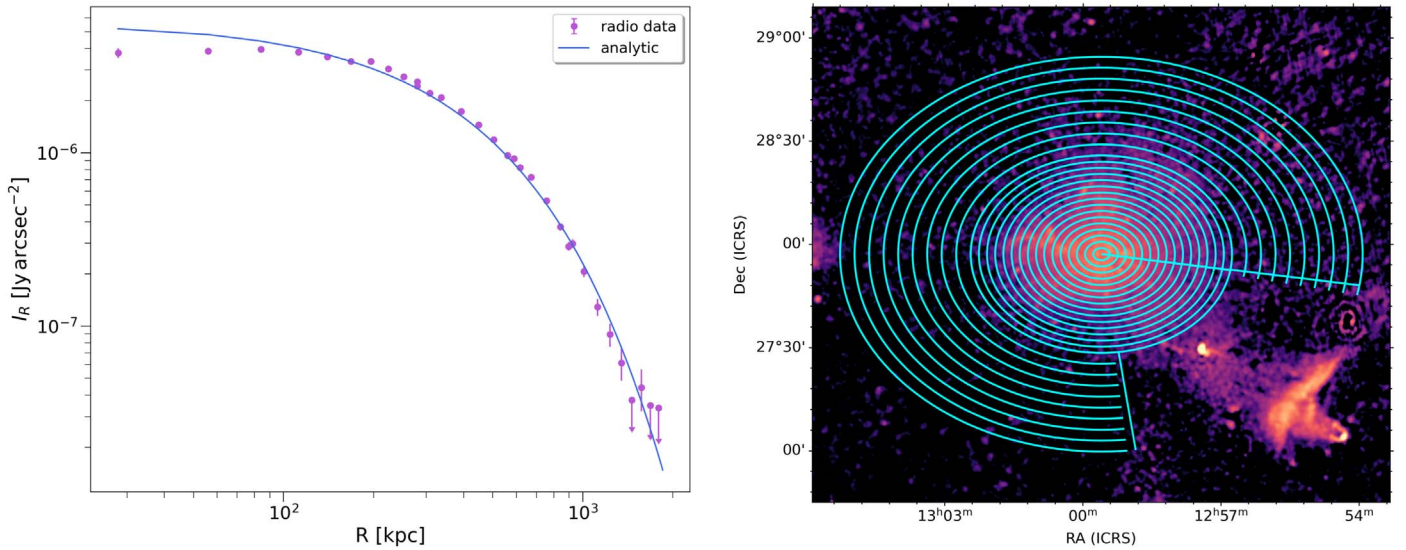


Figure 8. Left panel: circles are the radio average brightness profile of the radio halo, computed within elliptical annuli having major- and minor-axis sub-multiples and multiples of r_1 and r_2 , i.e., the minor and major axis of the elliptical exponential fit (see Table 4). The SW sector of the halo has been blanked for ellipses with major and minor axis larger than $3r_1$ and $3r_2$, respectively, to exclude the bridge region. Error bars represent the error on the mean; upper limits at 3σ are plotted as arrows. The width of the annuli goes from $1'$ in the center to $4'$ in the outer annuli, to improve the sensitivity to low surface brightness emission in the outer parts of the halo. The blue line refers to the best-fit elliptical model; see Table 4. Right panel: radio image of the Coma cluster at $1'$ resolution. The inner cyan ellipse has major and minor axis equal to $3r_1$ and $3r_2$, respectively, and elliptical annuli are spaced by $1'$. The outer elliptical bins have a width of $4'$ and trace ellipses out to $6r_1$ and $6r_2$, showing the SW region that has been excluded from the analysis because of the bridge.

Table 4
Radio Halo 2D Fit

LOFAR—144 MHz									
Halo model	χ_r^2	I_0 ($\mu\text{Jy arcsec}^{-2}$)	r_1 (kpc)	r_2 (kpc)	r_3 (kpc)	r_4 (kpc)	Angle (deg)	$S_{144,\text{MHz}}$ (Jy)	$P_{144,\text{MHz}}$ ($10^{25} \text{ W Hz}^{-1}$)
Circular	1.7	5.42 ± 0.04	310 ± 1					12.20 ± 0.04	1.470 ± 0.002
Elliptical	1.6	5.50 ± 0.02	355 ± 1	268 ± 1				12.21 ± 0.04	1.470 ± 0.005
Skewed	1.6	5.46 ± 0.01	337 ± 2	368 ± 2	207 ± 2	342 ± 2	2.99 ± 0.001	12.35 ± 0.05	1.490 ± 0.05
WSRT—342 MHz									
Halo model	χ_r^2	I_0	r_1	r_2	r_3	r_4	Angle	$S_{342,\text{MHz}}$	$P_{342,\text{MHz}}$
Circular	0.7	3.52 ± 0.08	255 ± 4					5.3 ± 0.1	0.64 ± 0.01
Elliptical	0.7	3.54 ± 0.08	268 ± 5	240 ± 6				5.3 ± 0.1	0.64 ± 0.01

Note. Column (1): model used. Column (2): reduced χ^2 value. Column (3): central brightness of the fit. Columns (4)–(7): e -folding radii. Column (8): angle for the skewed halo model fit. Column (9): total halo power at 144 MHz computed within $3r_e$. Only statistical fit errors are shown in the table.

characteristic e -folding radius, and $r^2 = x^2 + y^2$. The skewed model allows for an off-center maximum of the brightness distribution and is characterized by four different scale radii (r_1 , r_2 , r_3 , r_4) and by an angle to describe the asymmetric brightness distribution.

We have investigated these three profiles (circular, elliptical, and skewed), and results of the fit are given in Table 4. In this table, we only list the statistical error, while the systematic one is 15% of the listed flux density and due to the uncertainty on the absolute flux scale. All models give a consistent total radio power ($P_{144\text{MHz}} \sim 1.47 \times 10^{25} \text{ W Hz}^{-1}$ computed within 3 times the e -folding radius) and central radio brightness ($I_0 \sim 5 \mu\text{Jy arcsec}^{-2}$). We note that the flux density and consequently the power measured by the fit are in perfect agreement with the estimate derived from the images above $2\sigma_{\text{rms}}$ (see Section 3). As the reduced χ^2 values are similar in the skewed and elliptical model, we consider the latter in the following analysis.

In Figure 8, we show the radial profile of the halo brightness at 144 MHz. We have computed the mean of the radio brightness and its error within elliptical annuli having a width that changes progressively from $1'$ in the center to $4'$ in the outer regions, to maximize the resolution at the center and the sensitivity to low surface brightness emission in the halo peripheral regions. The bridge region is excluded starting from elliptical annuli with major and minor axis larger than $3r_1$ and $3r_2$, respectively. We considered upper limits the values where we have a mean smaller than 3 times the rms noise. From this plot, we derive that we have detected the halo emission up to $r \sim 1.3 \text{ Mpc}$, which corresponds to $\sim 4.5r_1$ and r_2 (see Table 4).

In the following, we refer to the halo core as the emission contained within an ellipse having as major and minor axis r_1 and r_2 , respectively, and to the outer halo as the emission contained within $4r_1$ and $4r_2$, excluding the halo core. We note that the halo core and outer halo are well represented by a single exponential model and do not need to be considered as

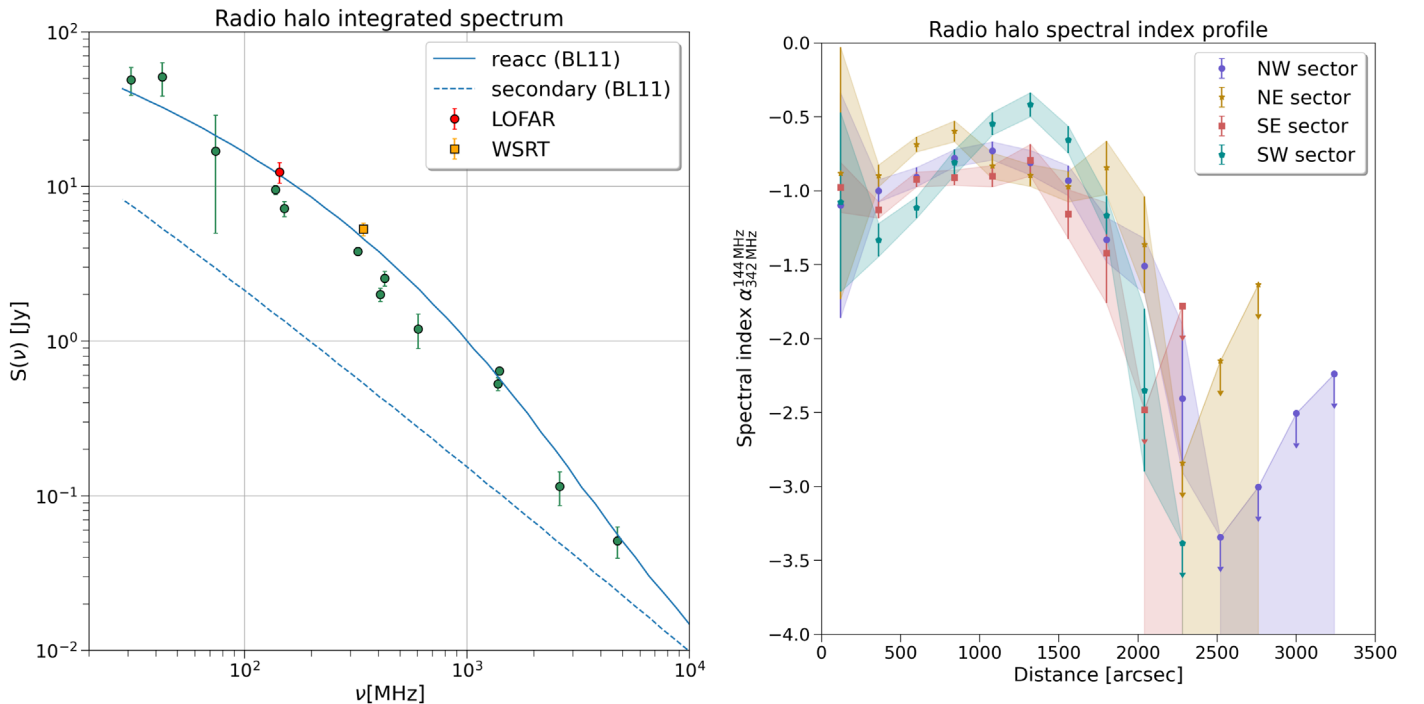


Figure 9. Left: integrated spectrum of the radio halo from literature data (green circles) from Thierbach et al. (2003 and references therein), as corrected and rescaled by Brunetti et al. (2013). The new LOFAR measurement (red circle) and the WSRT measurement (orange square) are shown, measured within 3 times the effective radii as derived by the halo fit (see text for details). The solid line shows expectations from a model where secondary particles are re-accelerated by compressive turbulence (Brunetti & Lazarian 2011). The dashed line shows the spectrum computed from secondary emission, after 200 Myr since turbulent re-acceleration has been switched off (Brunetti & Lazarian 2011). Right: spectral index radial profile computed in the different sectors, as listed in the legend. Arrows are 3σ upper limits, only statistical errors are shown, and the values of the spectral index are also affected by the flux calibration uncertainties of WSRT and LOFAR (10% and 15%, respectively) that would contribute with an additional error of 0.2.

two separate components, if we consider the average surface brightness of the halo emission. However, as we show in the following analysis, they are characterized by different properties.

We applied the same fitting procedure to the WSRT image (WSRT H in Table 2), after blanking the sources that were contaminating the emission. We only attempted an elliptical and circular model fit. Results are listed in the bottom part of Table 4. Both fits give the same total flux density and radio power and have the same χ_r^2 value, smaller than 1, possibly indicating that the errors are being overestimated. We note that the r_1 and r_2 values are slightly smaller than those found in the LOFAR image, indicating a more peaked profile of the radio emission and hence of the emitting CRE at higher frequencies.

5. Spectral Properties of the Radio Halo

5.1. The Integrated Spectrum

Using literature results and the halo flux density at 144 and 342 MHz, we can constrain the low-frequency part of the radio halo spectrum. The spectrum of radio halos provides important information about the underlying re-acceleration mechanism. Indeed, it allowed us in the past to conclude that a very steep spectrum ($\alpha < -1.5$, also called ultra-steep-spectrum halos) cannot be produced by hadronic models (e.g., Brunetti et al. 2008). Using the flux densities that result from the fits, we can measure the spectral index between 144 and 342 MHz, yielding $\alpha = -1.0 \pm 0.2$. Though residuals from sources could still be present, the fitting procedure we have used should minimize that contribution (Boxelaar et al. 2021); hence, a considerable

impact to the whole halo emission is unlikely. We find that the spectrum is slightly flatter than previously reported in the literature, although still consistent within the errors. The spectrum of the halo in the Coma cluster has been extensively studied in the literature (e.g., Giovannini et al. 1993; Thierbach et al. 2003), using both interferometric images and single-dish data. At low frequencies, the contribution of radio galaxies is difficult to account for, for mainly two reasons: (i) the low resolution of observations published so far, and (ii) the larger extent of tailed radio galaxies whose emission blends with the halo emission. Our sensitive and high-resolution LOFAR images allow us to alleviate both of these problems. In addition, we now have a more accurate method to estimate the halo flux density. We have collected the data available in the literature, i.e., those presented in Thierbach et al. (2003) and rescaled to the same absolute flux scale as in Brunetti et al. (2013), and added our measurement at 144 MHz. In Figure 9 we show the spectrum of the halo. Green circles refer to values taken from Brunetti et al. (2013) and do not refer to the same aperture radius. The red and orange circles refer to the LOFAR and WSRT maps, respectively, computed within the same aperture (corresponding to three e -folding radii of the LOFAR image; see Table 4). In Figure 9, left panel, we show one possible spectrum that would be produced by re-acceleration models. However, for a proper derivation of the halo spectral properties, one should compare the flux densities from images done with the same uv -range, the same procedure for compact source subtraction, and using the same aperture radius. We also note that using a fitting algorithm, such as the one proposed by

Boxelaar et al. (2021) and used here, would also minimize the effect of different noise obtained at different frequencies.

Recently, Rajpurohit et al. (2022) have shown that the hint for a spectral break claimed in the radio relic of A2256 below 1.4 GHz (Trasatti et al. 2015) is not confirmed once the analysis is performed with matching uv -coverage and unrelated sources are subtracted properly. In the case of the Coma halo, we note that the high-frequency measurements are almost a factor 10 below the value extrapolated from a power law at low frequencies. However, the exact shape of the spectrum could be affected by the effects mentioned above. In addition, it is important to get a precise flux density at frequencies below 100 MHz to characterize the integrated radio spectrum. Here data from the LOFAR Low-Band Antennas (LBA) will provide powerful constraints.

5.2. Spectral Index Profile

Using WSRT and LOFAR HBA data, we can obtain a radial profile of the halo spectral index. A steepening of the radial profile has been found by Giovannini et al. (1993) using data between 326 MHz and 1.38 GHz. They found that the radio halo has a smooth spectrum in the central regions (inner $480''$ radius) with $\alpha \sim -0.8$ and a steeper value ($\alpha \sim -1.2$ down to -1.8 in the outer regions).

Using WSRT and LOFAR HBA images, we can now compute the spectral index profile out to larger distances. We have reimaged the LOFAR data using only baselines larger than 40 m, i.e., the shortest WSRT baseline, and convolved the LOFAR image to the same resolution as the WSRT image. The sources embedded in the diffuse emission are subtracted from the WSRT image; however, as some residuals were still present, we applied the multi-filtering technique described in Rudnick (2002) and blanked the WSRT image wherever the filtered image was above 3 mJy beam^{-1} . We blanked the LOFAR image accordingly. We have divided the radio halo into four sectors (NW, NE, SE, and SW) and computed the mean spectral index α in elliptical annuli having the major and minor axis proportional to r_1 and r_2 , up to the maximum distance where the halo is detected (see Section 4 and Figure 8).

The four outermost annuli of the SW sector have been removed to exclude the bridge region. We have computed the spectral index in each annulus and considered upper limits the annuli that have a total flux density smaller than $3\sigma_{\text{rms}} \times \sqrt{N_{\text{beams}}}$, with N_{beams} being the number of independent beams sampled in each annulus. As the radio halo is more extended in the LOFAR image than in the WSRT image, we mainly derive upper limits at distances larger than $\sim 2000''$ (950 kpc). The radial trend of the spectral index is shown in the right panel of Figure 9. We note that values in some annuli are surprisingly flat, possibly because of residual contamination from unrelated sources. The increasing values of the upper limit in the outer annuli are due to the larger area sampled by the annuli. All the sectors show a spectral index that becomes steeper at distances of $\sim 1500''$ from the cluster center. In the SW sector, we also clearly detect a steepening toward the cluster center. A similar, though less pronounced, trend is also observed in the other sectors, though we note that in the NE sector the radial profile of α is more complex, and no clear trend at distances smaller than $r \sim 2000''$ can be established. The SW sector is affected by the passage of the NGC 4839 group; hence, is it possible that different physical conditions

are present there. Overall, we can conclude that the spectral trend is characterized by clear steepening at the cluster outskirts and a mild steepening toward the cluster center.

In the next section we will discuss the physical implications of these results in the framework of turbulent re-acceleration models.

5.3. Radial Variations of The Spectral Index and Re-acceleration Models

In the presence of a break in the integrated spectrum of radio halos, homogeneous re-acceleration models predict that increasingly steeper spectra will be seen at increasing distance from the cluster center (Brunetti et al. 2001). Assuming homogeneous conditions, the frequency at which steepening occurs, ν_s , is proportional to

$$\nu_s \propto \tau_{\text{acc}}^{-2} \frac{B}{(B^2 + B_{\text{IC}}^2)^2}, \quad (2)$$

where τ_{acc} is the re-acceleration time (see Cassano & Brunetti 2005; Brunetti & Lazarian 2007), which depends on the assumed turbulent properties and re-acceleration mechanism. B_{IC} is the inverse Compton equivalent magnetic field. In the case of a constant τ_{acc} , the steepening frequency depends only on the magnetic field strength. To better follow the discussion below, let us define a critical magnetic field value

$$B_{\text{cr}} = \frac{B_{\text{IC}}}{\sqrt{3}} \sim 2 \mu\text{G}.$$

As long as $B < B_{\text{cr}}$, one expects to see a radial steepening of the spectral index at distances larger and larger from the cluster center as we move toward lower observing frequencies. This is what we observe beyond a radius of $\sim 30'$. Giovannini et al. (1993) also detected a steepening between the higher frequency pair 325 MHz and 1.38 GHz, beyond a radius of $\sim 8'$ from the cluster center. While we do expect more dramatic steepening at the higher frequencies, whether these two sets of measurements are consistent with a single physical model requires further investigation.

Moreover, we detect for the first time a steepening of the spectral index toward the cluster center. This can also be explained in the framework of homogeneous re-acceleration models, if in the cluster center we have $B > B_{\text{cr}}$. Assuming a magnetic field profile as derived from rotation measure (RM) studies ($B \propto B_0 n_e^{0.5}$; Bonafede et al. 2010), we have indeed a central magnetic field of $B_0 \sim 5 \mu\text{G}$, and hence $B > B_{\text{cr}}$. We note that a similar steepening toward the cluster center should be visible also in the higher frequency spectral index map by Giovannini et al. (1993). However, in that work the authors only report a spectral index trend through a line passing from the cluster from SE to NW. It is possible that a radial analysis similar to the one we present here would show the same trend. Alternatively, one should think of ad hoc re-acceleration conditions that make this steepening visible only at low frequency. Future observations at higher frequencies could shed light on this point.

We can conclude that the data presented in this work, together with literature data by Giovannini et al. (1993) and Bonafede et al. (2010) provide a coherent picture with the expectations from homogeneous turbulent re-acceleration models (Brunetti et al. 2001), though the spectral index trend

in the cluster center leaves some open questions that could be addressed by future observations.

5.3.1. Toward a Constraint of The Re-acceleration Model Parameters

Constraining the model parameters, such as τ_{acc} , would require a detailed 3D modeling and a precise constraint on the radial position of ν_s . However, we can try to make first-order calculations to see whether the qualitative coherent picture outlined above is quantitatively supported. Giovannini et al. (1993) have detected a spectral steepening at $\sim 8'$ between 326 MHz and 1.38 GHz. Assuming a central magnetic field $B_0 = 4.7 \mu\text{G}$, one would expect to detect the steepening between 144 and 342 MHz, where the magnetic field is $B \sim 0.7 \mu\text{G}$, i.e., at $r \sim 2 \text{ Mpc}$ ($\sim 71'$) from the cluster center. Instead, the steepening is detected at $r \sim 30'$ from the cluster center, i.e., a factor 2 closer to the expected location. This may suggest that τ_{acc} is not constant and increasing with the distance from the cluster center. Though this result is not surprising from a theoretical point of view, it would be the first time that data support this claim. Instead of a constant τ_{acc} , we can make a step further and assume a constant turbulent Mach number \mathcal{M}_t . In this case, the steepening frequency is proportional to

$$\nu_s \propto T^{2a} \frac{B}{(B^2 + B_{\text{ICM}}^2)^2}, \quad (3)$$

where T is the cluster temperature and a is a constant that is $a = 1$ for re-acceleration via Transit-Time-Damping mechanism with compressive turbulence and $a = 1.5$ for non-resonant second-order acceleration with solenoidal turbulence²⁰ (Brunetti & Lazarian 2016). In order to explain the spectral index steepening at $r \sim 30'$ from the cluster center, the temperature should be $\sim 35\text{--}45\%$ lower at a distance of $30''$ than at a distance of $8''$, where the steepening is detected at higher frequency. We note that this temperature drop is consistent with the temperature profile found by Simionescu et al. (2013).²¹ We stress again that the calculations we have just performed do not allow us to make any claim, as long as ν_s is not precisely determined from data and projection effects are not taken into account. However, they show that the qualitative picture outlined above is not at odds with first-order quantitative estimates.

6. Thermal and Non-thermal Correlations in the Radio Halo

6.1. Point-to-point Analysis

Investigating the point-to-point correlation between the radio and the X-ray surface brightness can give important information about the relation between the thermal and non-thermal components of the ICM. In addition, it has the potential of constraining the mechanism responsible for the radio emission. Govoni et al. (2001) have first investigated this correlation for a small sample of radio halos, finding a sublinear scaling of the radio brightness with respect to the X-ray brightness. More recently, Botteon et al. (2020a), Rajpurohit et al.

²⁰ In this case we consider also a constant Alfvén velocity, based on the scaling $B^2 \propto n$.

²¹ We take as a reference the profile extracted along the east sector of their analysis, which is the only one not contaminated by the west shock and by the merger with the NGC 4839 group.

Table 5
Radio–X-ray Correlation for Different Gaussian Smoothing Lengths

Gaussian Beam	β	10%–90%	ρ_P
FWHM			
1'	0.64	0.65–0.63	0.86
2'	0.65	0.66–0.63	0.88
3'	0.68	0.70–0.66	0.89
4'	0.70	0.73–0.68	0.88
5'	0.74	0.78–0.70	0.89
6'	0.76	0.81–0.72	0.88

Note. Column (1): FWHM of the smoothing Gaussian or restoring beam. Column (2): best-fit slope. Column (3): 10th and 90th percentile of the posterior distribution for β . Column (4): Pearson correlation coefficient.

(2021a, 2021b), and Ignesti et al. (2020) have investigated the same correlation for radio halos and mini halos, respectively, finding that halos tend to have a sublinear or linear scaling and mini halos show linear or superlinear behaviors.

Since the Coma radio halo is the one for which most spatially resolved and multiwavelength data are available, it is important to establish the statistical relation between its thermal and non-thermal components.

We have investigated the thermal to non-thermal correlation for the Coma cluster, fitting the radio (I_R) and X-ray (I_X) surface brightness in log–log space, according to

$$\log I_R = \beta \log I_X + \gamma, \quad (4)$$

where β is the correlation slope. We have used a hierarchical Bayesian model (Kelly 2007), which allows us to perform linear regression of I_R on I_X accounting for intrinsic scatter in the regression relationship, possibly correlated measurement errors, and selection effects (e.g., Malmquist bias). Using this method, we have derived a likelihood function for the data. We consider the mean of the posterior distribution as the best-fit slope. Following Botteon et al. (2020a) and Bonafede et al. (2021), we considered as upper limits the radio values that are below $2\sigma_{\text{rms}}$.

Despite the fact that we detect the radio halo up to a distance of $\sim 1.3 \text{ Mpc}$, the analysis of the radio–X-ray correlation is limited by the extent of the XMM-Newton mosaic. In particular, because of soft-proton contamination, the analysis is restricted to a distance of $2400''$ ($\sim 1.1 \text{ Mpc}$) from the cluster center. To gain sensitivity toward the low surface brightness emission of the halo outskirts, we have convolved the radio image with Gaussian beams having FWHM of $1', 2', 3', 4', 5',$ and $6'$. We have computed the mean of the radio and X-ray brightness in square boxes having an area equal to a Gaussian beam of the radio image and computed the fit using X-ray images smoothed at the same resolution. We have considered upper limits the values that are below $2\sigma_{\text{rms}}$, i.e., twice the noise of the radio image. The results of the fits are listed in Table 5 and the I_X – I_R correlation from the image at $6'$ resolution is shown in Figure 10. The image at $6'$ resolution allows us to recover the outermost regions of the halo keeping the highest possible resolution. I_X and I_R are positively correlated with a slope $\beta = 0.76^{+0.05}_{-0.04}$ and a Pearson correlation coefficient $\rho_P = 0.89$. We note that the finest grid (boxes spaced by $1''$) recovers a slope similar to the one initially found by

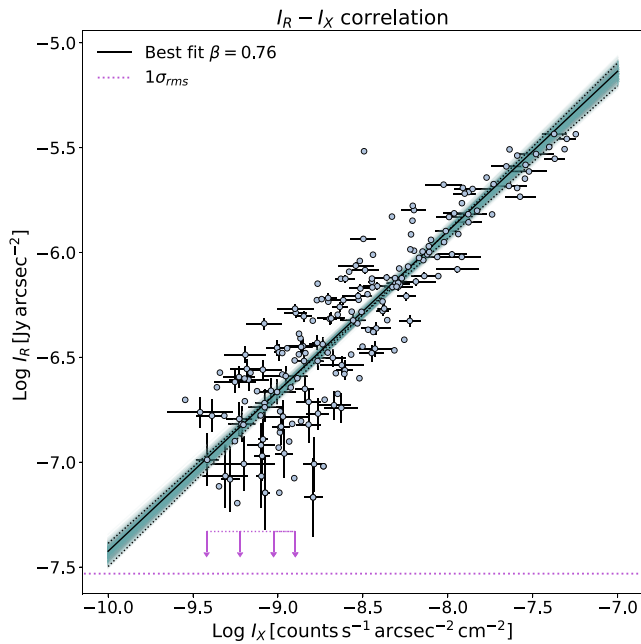


Figure 10. I_R - I_X correlation computed from the $6'$ image using cells equally spaced by $6'$. Arrows mark the $2\sigma_{\text{rms}}$ upper limits, the black solid line shows the best-fit line, and dotted lines show the 10% and 90% slopes for the posterior distribution of β . The magenta dotted horizontal line marks the $1\sigma_{\text{rms}}$. All data are computed within $2400''$ from the cluster center. Here and in the following correlation plots, error bars are plotted every second point for clarity reasons.

Govoni et al. (2001). The slope increases as we gain sensitivity to the low surface brightness emission that characterizes the outermost regions of the radio halo. This is suggesting that the slope of the correlation is not constant throughout the radio halo, with the slope β increasing when low surface brightness emission is added.

6.2. Correlations in the Halo Core and Outer Halo

Our analysis suggests that the point-to-point I_R - I_X correlation may be different in the halo central regions and in their outskirts.

Recent low-frequency observations have found radio emission in galaxy clusters that can be interpreted as the coexistence of a mini halo in the cluster core and a giant halo on larger scales (Savini et al. 2019; Biava et al. 2021). A different I_R - I_X trend is found in the core and in the outer part of the halo of these clusters, with a superlinear scaling in the mini halo region and a sublinear scaling in the outer part (Biava et al. 2021; G. Lusetti et al. 2022, in preparation).

Although those clusters have a cool-core and a radio halo with a steep spectrum, we note that a change in the I_R - I_X correlation slope for radio halos has never been explicitly investigated in the literature. In the cluster A2142, a radio halo with two components has been found (Venturi et al. 2017), yet no analysis of the radio and X-ray correlation has been performed so far. In addition, in the cluster A2744, a multicomponent halo has been discovered with a different radio-X-ray correlation slope for the northern and southern components (Rajpurohit et al. 2021b).

Since a point-to-point analysis of radio and X-ray surface brightness has been so far presented only for a few clusters, we investigate whether or not the different trends observed in the core and in the outer part of the Coma halo can be a common

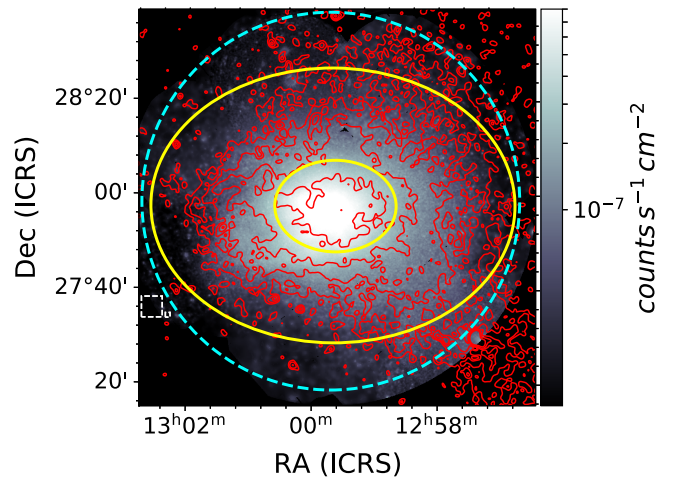


Figure 11. Left panel: colors are the X-ray emission from the Coma field from XMM-Newton observations. Contours show the radio emission at $1'$ resolution, starting at $3\sigma_{\text{rms}}$ and increasing by a factor 2. The major axes of the ellipses are r_1 and r_2 (inner ellipse) and $3r_1$ and $3r_2$ (outer ellipse). r_1 and r_2 are listed in Table 4. The inner ellipse is the region considered for the “halo core.” The cyan dotted circle marks the region that is not contaminated by soft X-ray protons.

property of radio halos. We have repeated the analysis described in Section 6 considering the “halo core” and the “outer halo” separately (see Figure 11). For the halo core, we have used the finest grid of $1'$ cell size, while for the outer halo we have used the $6'$ grid, to recover the faintest emission.

We find that the slope of the “halo core” is $\beta = 0.41^{+0.04}$, while for the “outer halo” we find $\beta = 0.76 \pm 0.05$.

Hence, we can conclude that in the “halo core” we find a flatter slope for the I_R - I_X correlation, with respect to the outer part, which is the opposite trend found in cool-core clusters that host a mini halo and a halo-type component (e.g., RXC J1720.1+2638, Biava et al. 2021; A1413, G. Lusetti et al. 2022, in preparation). We note that this is the first time that a change in the I_R - I_X correlation has been investigated; hence, it could be a common property of radio halos. This result indicates that the inner part of the Coma radio halo has different properties than mini halos observed in more relaxed clusters, likely indicating different local plasma conditions. In particular, the detection of a sublinear trend in the brightest part of the halo hints at a negligible contribution to the halo central emission from the hadronic mechanism.

6.3. Radial Analysis

The point-to-point analysis above is important to understand the local connection between thermal and non-thermal plasma, and allows one to understand whether regions with higher non-thermal energy are traced by high X-ray brightness. The point-to-point analysis has also been used to probe the radial scaling of the radio and X-ray brightness (e.g., Govoni et al. 2001; Botteon et al. 2020a). To better analyze the radial trend of I_X and I_R and to investigate a possible change with radius, we have performed an additional analysis by comparing the X-ray and radio brightness in elliptical annuli and dividing the radio halo into sectors. Specifically, we have excluded from the analysis the SW sector, where the bridge is, and we have considered separately the NW, NE, and SE sectors. The profiles are computed in elliptical annuli with progressively increasing width to gain sensitivity toward low surface brightness emission in the halo outermost regions. X-ray profiles have

been computed using the same regions. These plots, shown in Figure 12, show a different radio profile in the three sectors we have considered and show clearly a shallower decline of the radio brightness with respect to the X-ray brightness. In the NW sector, we detect a sharp decline of the radio brightness at $\sim 1900''$ i.e., the location of the radio front (see Section 9). In the NE sector a sharp decline of the radio emission is detected at $\sim 1400''$ (670 kpc). This is due to the presence of the filaments of the radio halo (Figure 3) and to the asymmetry of the halo emission, which is more pronounced toward the W. The radio profile in the SE sector shows, instead, a smooth decline.

To inspect the possible change in the relative radial trend of I_R and I_X , we show in the top panel of Figure 13 the ratio I_R/I_X in logarithmic base-10 scale, for the different sectors (NW, NE, and SW). The trend is similar in the three sectors, with a ratio that is smaller in the central part of the halo and that progressively increases. In the three outermost annuli (approximately at $1600''$, i.e., ~ 750 kpc) the ratio decreases in the NE and SE sectors. This plot shows that the ratio of the two quantities is not constant throughout the halo, consistent with the results obtained in the point-to-point analysis. In the middle panel of Figure 13, we show the ratio of I_R to I_X^β , using the value of β obtained from the point-to-point analysis ($\beta = 0.76$). If the same value of β were representative of the whole halo, we would expect to see a horizontal line. Instead, the plot shows that a single value of β does not represent the whole halo emission. The change in the slope of β is shown more clearly in the bottom panel of Figure 13, where we plot $I_R/I_X^{\beta_{\text{core}}}$, where $\beta_{\text{core}} = 0.41$ is the best-fit value obtained from the point-to-point analysis restricted to the halo core.

Hence, we conclude that the I_R - I_X correlation has a slope that changes with the radial distance from the cluster center, being flatter in the halo core (where we find $\beta \sim 0.41$) and steeper in the outer halo (where we find $\beta \sim 0.76$). While the slope in the core seems to remain constant, the ratio I_R/I_X^β , shown in the middle panel of Figure 13, indicates a progressive steepening of the correlation with increasing distance from the cluster center.

6.4. Modeling the I_R - I_X Correlation and Its Radial Trend

A steepening of the I_R - I_X correlation outside the core is expected as a consequence of the different relative weight of inverse Compton and synchrotron losses in a magnetic field declining with radius. Hence, under some assumptions on the magnetic field profile, we can investigate whether the expected radial drop of magnetic field can be entirely responsible for the steepening of the correlation, or whether additional effects are required. We assume a magnetic field profile scaling with the thermal gas as $B(r) \propto B_0 \cdot n_e(r)^{0.5}$, consistent with Bonafede et al. (2010). Note that in this case the Alfvén velocity in the ICM is constant. The radio emissivity in turbulent re-acceleration models can be expressed as

$$\epsilon_R \propto F \eta_e \frac{B^2}{B^2 + B_{\text{IC}}^2}, \quad (5)$$

where η_e is the acceleration efficiency, B_{IC} is the CMB equivalent magnetic field, and F is the turbulent energy flux,

$$F \sim \frac{1}{2} \rho \frac{\sigma_v^3}{L}. \quad (6)$$

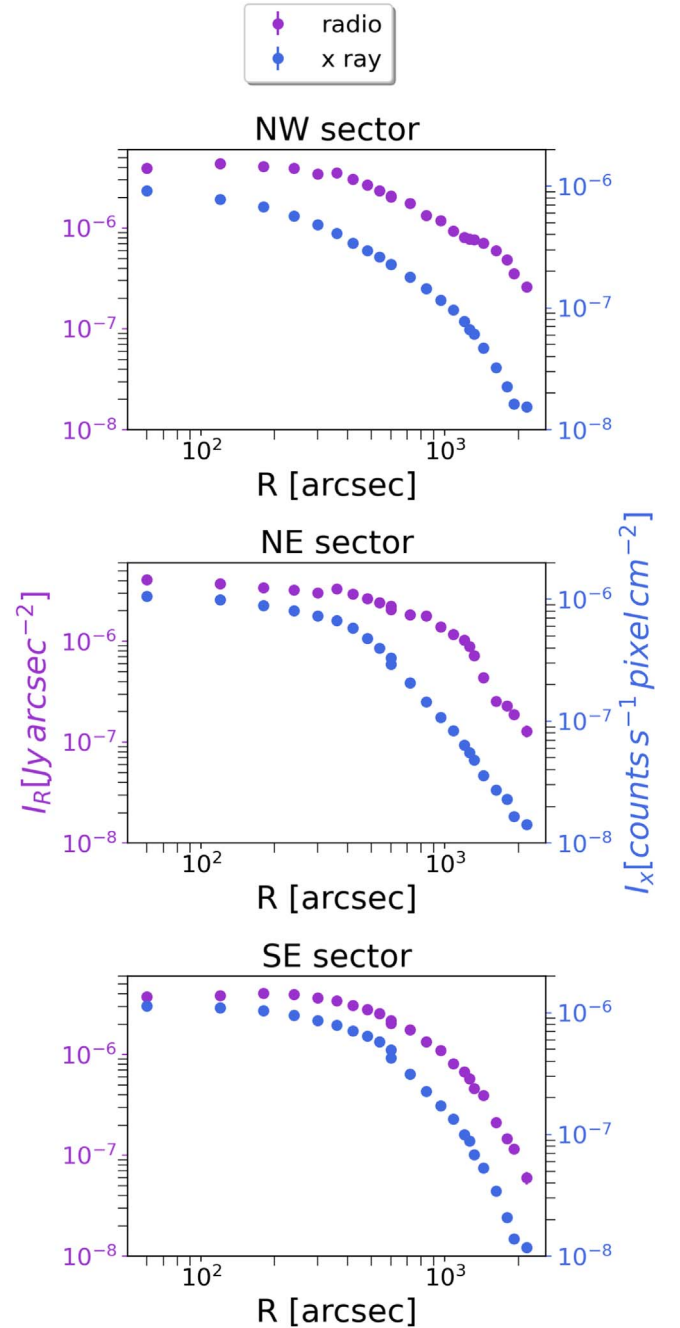


Figure 12. Radial profile of the X-ray brightness and radio brightness in the NW, NE, and SE sectors (top to bottom). The profiles are computed in elliptical annuli with different width from the center to the outermost regions as specified in Figure 8, but excluding the SW sector and dividing the remaining area into three sectors. The outermost annulus in the NW sector shows contamination from soft X-ray protons and has been excluded from the following analysis. Statistical error bars do not appear, as they are smaller than the points.

Here σ_v is the velocity dispersion on scale L , and ρ is the gas density. Assuming an isotropic distribution of electrons in the momentum space, $f(p)$, the acceleration efficiency is (e.g., Brunetti & Lazarian 2007)

$$\eta_e \sim F^{-1} \int d^3p \frac{E}{p^2} \frac{\partial}{\partial p} \left(p^2 D_{pp} \frac{\partial f}{\partial p} \right) \approx \frac{U_{\text{CRE}}}{F} (D_{pp}/p^2), \quad (7)$$

where U_{CRE} is the energy density of re-accelerated electrons and D_{pp}/p^2 has different expressions in different re-

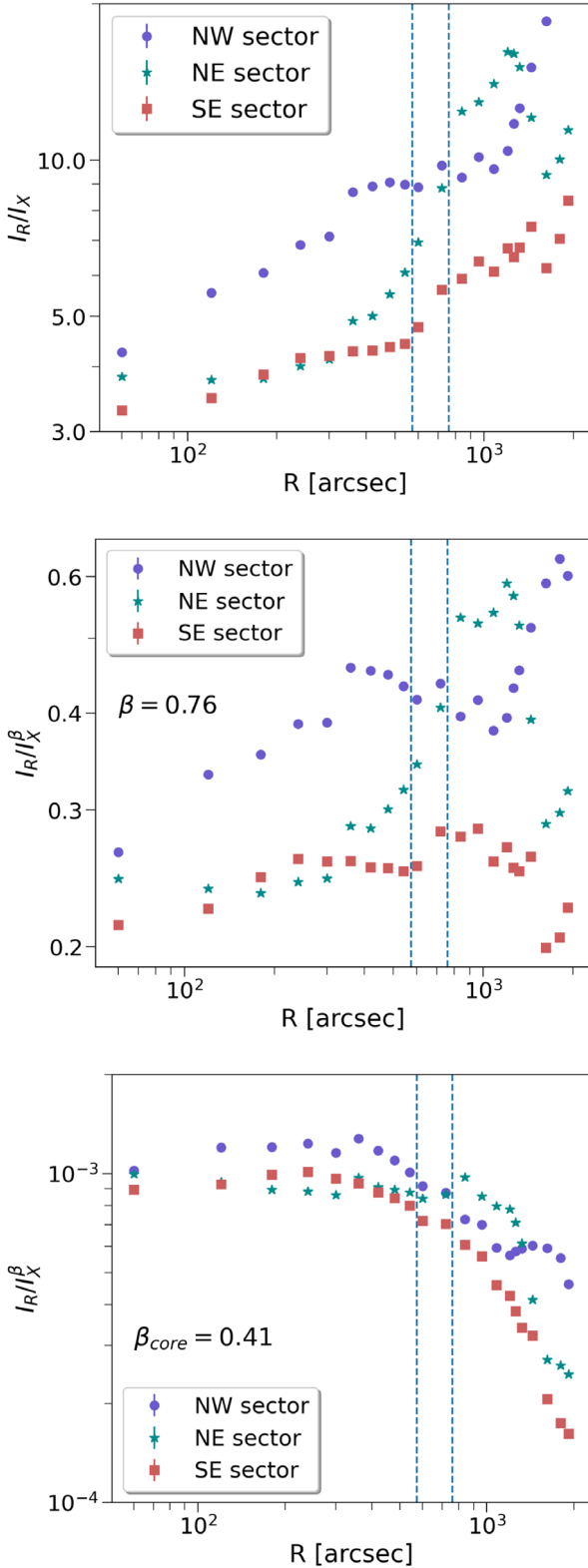


Figure 13. Top: ratio of the radio to X-ray brightness, computed in elliptical annuli as in Figure 12. Middle: ratio of I_R/I_X^β , where $\beta = 0.76$ is the best-fit correlation coefficient found for the whole halo. Bottom: ratio of $I_R/I_X^{\beta_{\text{core}}}$, where $\beta_{\text{core}} = 0.39$ is the best-fit correlation coefficient found for the halo core. In the three panels, circles, stars, and squares refer to the NW, NE, and SE sector, respectively. Vertical dashed lines mark the position of r_1 and r_2 , used to separate the halo core from the outer halo. Statistical error bars do not appear, as they are smaller than the points.

acceleration models. Specifically,

$$\frac{D_{pp}}{p^2} \propto \frac{c_s^2 \mathcal{M}_t^4}{L} \quad (8)$$

in the case of Transit-Time-Damping acceleration with compressive modes (Brunetti & Lazarian 2007; Miniati & Beresnyak 2015) and

$$\frac{D_{pp}}{p^2} \propto \frac{c_s^3 \mathcal{M}_t^3}{L v_A} \quad (9)$$

in the case of non-resonant second-order Fermi acceleration with solenoidal modes (Brunetti & Lazarian 2016). If we also assume a constant temperature and a scenario based on a constant turbulent Mach number, the synchrotron emissivity is

$$\epsilon_R(r) = \epsilon_R(0) \frac{X(r)}{X(0)} \left(\frac{\epsilon_X(r)}{\epsilon_X(0)} \right)^{\frac{1}{2}} \frac{1 + \left(\frac{B_{\text{IC}}}{B_0} \right)^2}{1 + \left(\frac{B_{\text{IC}}}{B(r)} \right)^2 \left(\frac{\epsilon_X(0)}{\epsilon_X(r)} \right)^{\frac{1}{2}}}, \quad (10)$$

where $\epsilon_X \propto n^2$ is the X-ray (bremsstrahlung) emissivity and $X = \frac{U_{\text{CRE}}}{U_{\text{th}}}$ the ratio of the energy density of CRE to thermal gas. From the radio and X-ray emissivity, we have computed the projected radio brightness assuming constant X and different values of the central magnetic field, B_0 , ranging from 3 to 10 μG and the X-ray brightness using the parameters obtained by Briel et al. (2001). Then, we have computed the slope of the correlation $I_X - I_R$ as a function of the radial distance from the cluster center. The trend of β versus the radial distance is shown in Figure 14 for different values of B_0 . We have overplotted as shaded areas the values obtained in the halo core and in the outer halo.

Although all the models predict a steepening of the radio–X-ray scaling with radius, none of them are able to reproduce all observed values. In particular, except for the profile with $B_0 = 5 \mu\text{G}$, the magnetic field profiles that would be compatible with the value of β in the outer halo are higher than those derived from RM studies (Bonafede et al. 2010). Although the central magnetic field derived from RM studies relies on several assumptions, models with a central magnetic field larger than $B_0 > 7 \mu\text{G}$ were unable to reproduce the observed trend of RM and RM dispersion (σ_{RM}). Hence, we discard the possibility of $B_0 > 10 \mu\text{G}$ to account for the discrepancy between observations and expectations in Figure 14. More likely, a possible scenario to explain the observed trend is to assume that the ratio of the CRE to thermal gas energy densities (X) increases with radial distance from the cluster center. This is indeed expected, as the lifetime of CRE in the ICM increases with the distance from the cluster center owing to the lower Coulomb and synchrotron losses. However, it is the first time that a radially decreasing X seems to be suggested by observational data.

As for the calculations done in Section 5.3.1, we stress that the calculations outlined here are subject to several assumptions and the decrease of X with the distance from the cluster center is only one of the possible causes of the observed $I_R - I_X$ slope.

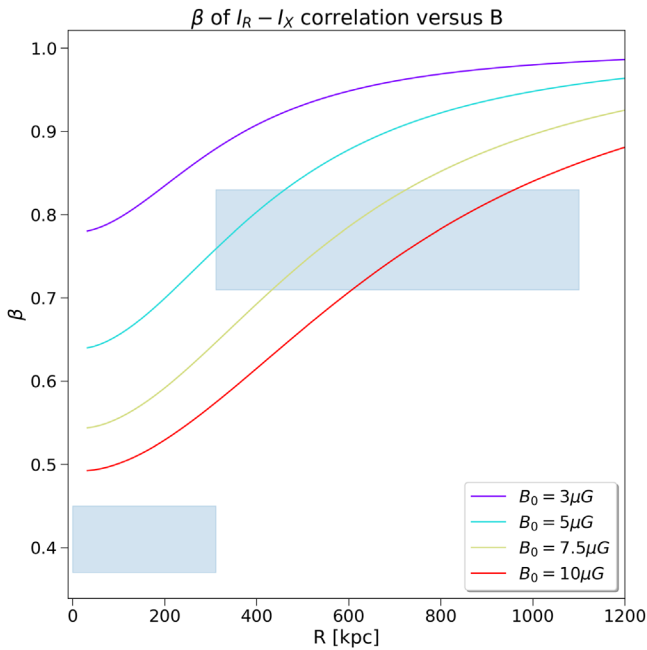


Figure 14. Trend of the radio–X-ray correlation slope β ($I_R = I_X^\beta$) with radial distance from the cluster center. β is computed as the ratio of the logarithm of the theoretical projected radio emissivity to the logarithm of the X-ray projected emissivity. The radio emissivity is computed for different values of the central magnetic field B_0 , from 3 (top curve) to 10 μG (bottom curve), as specified in the legend. The shaded area refers to the best-fit β obtained from data.

7. Radio–Thermal Pressure Correlation in the Radio Halo

Resolved SZ maps of the Coma cluster (Planck Collaboration et al. 2013) can be used to understand the connection between the thermal gas and the radio emission. Since the Comptonization parameter y is proportional to the gas pressure integrated along the line of sight ($y \propto n_e T$), it is less contaminated by cold gas clumps with respect to X-ray emission. We have computed the I_{SZ} – I_R point-to-point correlation, following the same approach as described above for the I_R – I_X correlation. We have used the radio image convolved to $5'$ resolution, to match the y -map resolution.

Initially, we have fit I_{SZ} versus I_R in the same region as the one considered in the I_R – I_X correlation, finding a superlinear slope $\beta_{SZ} = 1.76 \pm 0.08$. Assuming an isothermal model, one would expect that the value found from the I_{SZ} – I_R correlation would be twice the scaling of the I_R – I_X correlation. Hence, given the values found from the I_R – I_X correlation, one would expect $\beta_{SZ} = 1.4$ – 1.6 . There is a small tension between SZ and X-ray, which could be due, e.g., to dense and cold X-ray clumps in regions of low surface brightness emission. Understanding the details of this small tension is beyond the scope of this work; what is relevant for our analysis is that regions of high non-thermal energy are regions of high thermal energy, as probed by the I_{SZ} – I_R correlation.

The y -map is more extended than the XMM-Newton mosaic and covers regions at the cluster outskirts, where we have a radio halo detection. Hence, we can use the y -parameter map to investigate the correlation between thermal and non-thermal regions up to larger radii from the cluster center, though we miss the resolution given by X-ray data. We have fitted I_{SZ} versus I_R out to a distance of ~ 1.3 Mpc ($\sim 2800''$ radius) from the cluster center, which is the maximum distance where we

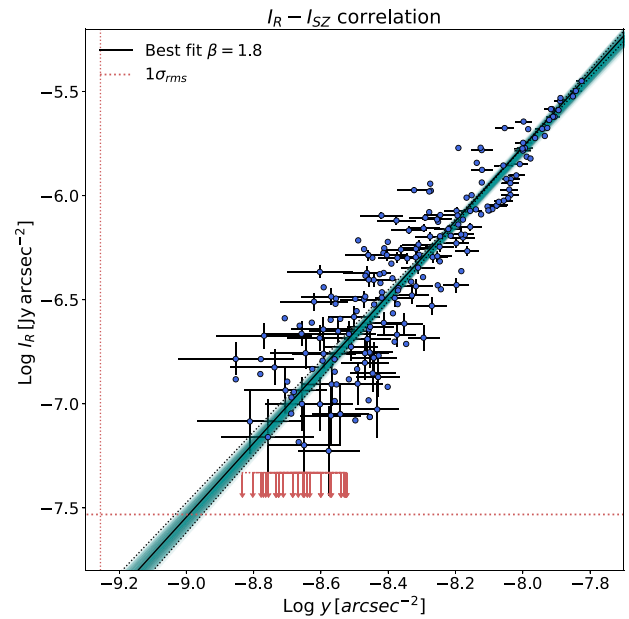


Figure 15. Radio–SZ correlation for the radio halo. The radio image has been convolved to a resolution of $5'$, and the source NGC 4839 has been masked. The error bars refer to the statistical errors of the two quantities. Arrows mark the $2\sigma_{rms}$ upper limits. The vertical and horizontal dotted lines mark $1\sigma_{rms}$ for the y -parameter and radio image, respectively. Error bars are plotted every second value.

have detected the radio halo. As shown in Section 6, we have an indication from the X-ray analysis that the slope would further increase when outer regions of the halo are considered. We find $\beta = 1.78 \pm 0.08$, which is slightly steeper than the slope found in the inner $2400''$ radius, though consistent within the errors. The I_{SZ} – I_R correlation is shown in Figure 15. Both X-ray and SZ analyses show that when outer regions of the halo are considered, the correlation slope increases, i.e., the outermost regions of the radio halo have a different ratio of thermal/non-thermal energy than the inner ones.

A correlation between the radio emission and the y -signal has been first obtained by Planck Collaboration et al. (2013), who fitted I_{SZ} versus I_R , finding a quasi-linear relation: $I_{SZ} \propto I_R^{0.92 \pm 0.04}$, which would correspond to our $\beta \sim 1.1$. They used the WSRT 325 MHz map and y images at $10'$ resolution and extracted the radio and y -signal from $r < 50'$ region. As we find a steeper slope, using a lower-frequency radio image, we investigate in the following the possible causes of the different trend. First of all, we are looking at the I_R – I_{SZ} correlation using a radio image at a different frequency than used in Planck Collaboration et al. (2013). In addition, we are able to perform a more accurate subtraction of the contaminating sources, as the highest LOFAR resolution is $6''$, and we are less affected by calibration artifacts than the WSRT image. Residuals from contaminating sources would increase the values of the radio brightness in each box, and this effect could be more prominent for boxes at the halo periphery. In this case, the effect would be a flattening of the correlation. The data we have at the moment of writing do not allow us to exclude that this is the cause of the different slope found with LOFAR and WSRT. However, we note that a higher value of the correlation slope for the I_R – I_X at lower frequencies has recently been found by Rajpurohit et al. (submitted) in the halo of the cluster A2256 and by Hoang et al. (2021) in the halo of CIG 0217+70.

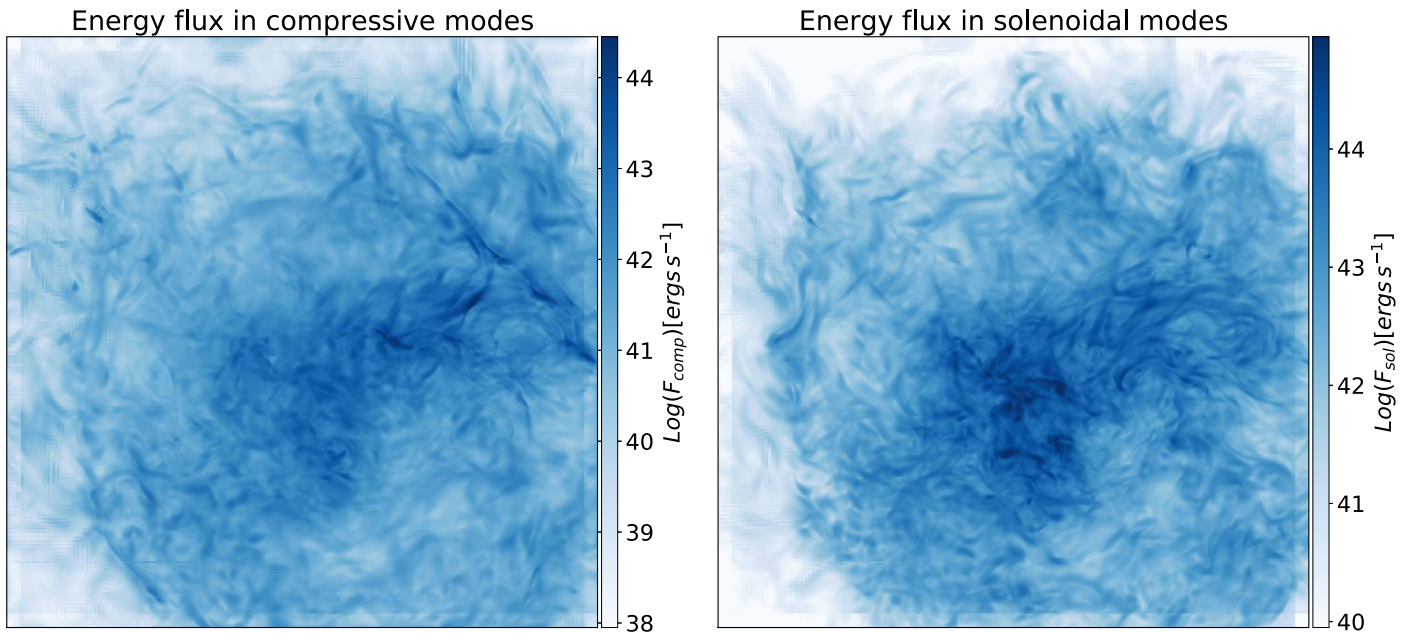


Figure 16. Projected F_{comp} (left) and F_{sol} (right) from MHD cosmological simulations of a Coma-like cluster, from Vazza et al. (2018). Each map has a size of 2560 kpc.

8. Comparison with Numerical Simulations

Having the radio halo resolved in great detail, we can try to understand its origin with the help of numerical simulations. Specifically, we try in this Section to understand whether the observed scaling I_R-I_X can provide useful information to better constrain the particle acceleration mechanism.

8.1. Simulated Thermal to Non-thermal Correlations

We use a Coma-like galaxy cluster, simulated at high resolution and with ideal magnetohydrodynamics using the cosmological Eulerian code ENZO (enzo-project.org) by Vazza et al. (2018). This system has a $z \approx 0.02$ total mass comparable with the real Coma Cluster, and it shows a radial decline of the magnetic field compatible with the estimates from RMs (Bonafede et al. 2010; Vazza et al. 2018). The simulation includes eight levels of adaptive mesh refinement (AMR) to increase the spatial and force resolution in most of the innermost cluster volume, down to $\Delta x = 3.95$ kpc per cell. While this simulation assumes an initial volume-filling background of weak magnetic field, $B_0 = 10^{-4} \mu\text{G}$ (comoving) at $z = 40$, the low-redshift properties of the magnetic field are fairly independent of the exact origin scenario, due to the effect of the efficient small-scale dynamo amplification (e.g., Donnert et al. 2009; Vazza et al. 2021). Using the filtering technique described in Vazza et al. (2017), we have computed the turbulent energy flux, $F_{\text{Comp,Sol}}$, associated with the compressive and solenoidal velocity components:

$$F_{\text{Comp,Sol}} = \rho \frac{\sigma_{\text{vComp,Sol}}^3}{L} \times \frac{B^2}{B^2 + B_{\text{IC}}^2}, \quad (11)$$

where, similarly as in Equation (6), $\sigma_{\text{vComp,Sol}}$ is the dispersion of the compressive, solenoidal velocity field on scale L , different for solenoidal and compressive modes. From F , one can compute the simulated synchrotron luminosity (see

Equation (5)) as

$$L_{\text{Comp,Sol}} = \eta_e F_{\text{Comp,Sol}}. \quad (12)$$

The constant $\eta_e \leq 1$ gives the dissipation efficiencies for solenoidal and compressive modes into cosmic-ray acceleration, which depend on the complex physics of cosmic-ray acceleration via the Fermi II process (see, e.g., Miniati & Beresnyak 2015; Brunetti & Lazarian 2016; Brunetti & Vazza 2020). However, since in this application to our new LOFAR observations of Coma we are only concerned with the relative distribution of the two energy fluxes, we fix η for simplicity, acknowledging that both fluxes will represent an overestimate (likely by a factor $\geq 10^2$) of the effective dissipation onto cosmic-ray acceleration. Hence, we have used $F_{\text{Comp,Sol}}$ as a proxy for the synchrotron luminosity instead of $L_{\text{Comp,Sol}}$. The maps of projected F_{Comp} and F_{Sol} are shown in Figure 16. We have computed the correlation between $F_{\text{Comp,Sol}}$ and the simulated X-ray brightness I_X as we have done for the radio and X-ray emission.

As we want to compare the observed scaling between I_R and I_X with simulated quantities, we have checked that we are not affected by different trends of I_X in the simulation with respect to observations. In Figure 17, we show the X-ray radial profiles obtained from observations and simulations, computed in the energy band 0.5–2 keV. The observed and simulated profiles have been rescaled to better compare the radial trends, that taking errors into account, results are consistent, and hence will not affect the comparison between simulated and observed thermal to non-thermal properties.

We note that some assumptions must be made to compare the simulated $F_{\text{Comp,Sol}}$ to the observed radio emission. Specifically, we have assumed that the halo emission is generated by turbulent re-acceleration, and that η_e is constant throughout the cluster volume. Furthermore, as we are not modeling the CRe component, we have averaged $F_{\text{Comp,Sol}}$ on scales larger than the electron diffusion length at 144 MHz. The

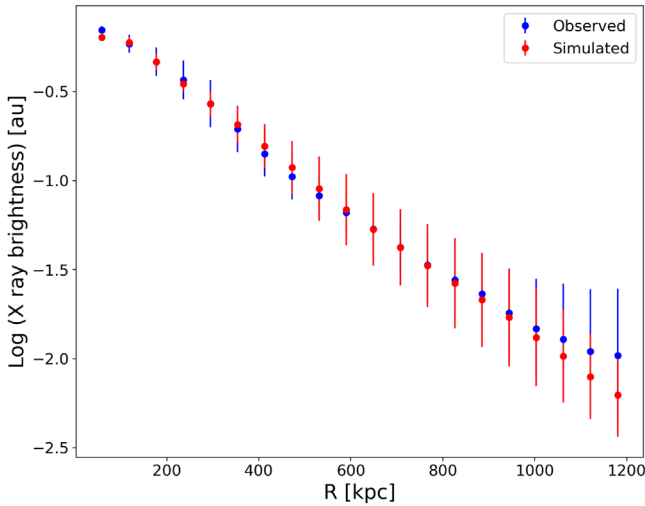


Figure 17. Simulated (red) and observed (blue) radial profiles of the X-ray brightness. The values have been computed in circular annuli. We plot the average (circles) and the standard deviation within each annulus (error bars).

diffusion length l_e of electrons emitting at 144 MHz can be estimated at first order as

$$l_e \sim 2\sqrt{D\tau_{\text{rad}}} \sim 100 \text{ kpc}. \quad (13)$$

Here τ_{rad} is the electrons’ radiative age at 144 MHz ($\tau_{\text{rad}} \approx 200$ Myr) and D is the spatial diffusion coefficient. A simple estimate for D (i.e., ignoring pitch-angle scattering along magnetic field lines) can be obtained from the typical scale for MHD turbulence in the ICM ($l_A \sim 0.1\text{--}0.5$ kpc) as $D \approx \frac{1}{3}l_A c$.

We have computed the mean of $F_{\text{Comp,Sol}}$ and I_X in boxes of 160 kpc a side, which is larger than l_e and comparable to the size of the boxes used to compute the I_R – I_X correlation from data (see Section 6).

In Figure 18, the two correlations obtained with simulated data are shown. Both F_{Comp} and F_{Sol} are positively correlated with the simulated I_X . The correlation slope is similar, though a bit steeper in the case of F_{Sol} – I_X (see Table 6). Both slopes are consistent with the observed I_R – I_X correlation, supporting the connection between turbulence and radio diffuse emission. We note that the power in the solenoidal energy flux is $\sim 10\%$ higher than in the compressive energy flux. Once the CRe emission is properly modeled, this could be used to disentangle the role played by the two modes for CRe re-acceleration.

8.2. Correlations in the Center and Peripheral Regions

As shown in the previous section, the global I_R – I_X in the Coma cluster can be recovered using both compressive and solenoidal energy fluxes as a tracer for the radio emission. MHD simulations show that solenoidal modes are dominant in the cluster central regions and compressive modes dominate the cluster outskirts (Miniati & Beresnyak 2015; Vazza et al. 2017). We have seen in Section 6 that the different β obtained in the halo core and in the outer halo cannot be explained by the decline of the magnetic field only. Here we investigate whether different turbulent modes could play a role. We have fitted the simulated $F_{\text{Comp,Sol}}$ versus the simulated X-ray brightness I_X in the cluster core and in the cluster external regions separately. We used boxes of 32 kpc size to have a better sampling of the halo core. The results are listed in Table 6.

The best-fit slopes for the outer halo are consistent with the global slopes. For the halo core alone, which samples a narrow region of I_X – $F_{\text{Comp,Sol}}$ space, the correlation is poor (Pearson correlator coefficient $\rho_P = 0.2\text{--}0.3$) and shows a formal fit for the slopes that is flatter than the others.

Hence, we conclude that globally the trends are in agreement with the scenario where turbulent re-acceleration produces the radio halo. In order to understand the process in more detail, the CRe distribution needs to be modeled.

8.3. Simulated Radio–SZ Correlation

Here we investigate the correlation between the simulated SZ signal and the values of F_{Comp} and F_{Sol} that we have considered as proxies for the radio emission. Following the same procedure detailed in the previous sections, we have computed the correlation between $F_{\text{Comp,Sol}}$ and the simulated SZ brightness, as we have done for the radio and SZ emission. The $F_{\text{Comp,Sol}}$ – y_{sim} correlations are shown in Figure 19. We find that the simulated SZ signal (y_{sim}) correlates with both F_{Comp} and F_{Sol} . Specifically, we find a superlinear slope $\beta_{\text{SZ}} = 1.8 \pm 0.1$ between F_{Comp} and y_{sim} , with a Pearson correlator coefficient of $\rho_P = 0.8$, and a slope $\beta_{\text{SZ}} = 1.9^{+0.1}_{-0.1}$ between F_{Sol} and y_{sim} (Pearson correlator coefficient $\rho_P = 0.8$). These trends are in very good agreement with the observed trend between y and I_R and support the idea that radio halos are powered by turbulence. As already noted for the simulated I_X – I_R correlation, it is possible that once the CRe distribution is properly modeled, the comparison between simulations and observations will yield information to determine which of the turbulent modes are responsible for particle (re)acceleration.

9. The Halo Front

Previous studies pointed out the presence of discontinuities in the thermal gas cluster properties located at the western edge of the radio halo (Markevitch 2010; Planck Collaboration et al. 2013; Simionescu et al. 2013). This discontinuity, detected in both the Comptonization parameter y and the temperature and deprojected density profiles, is consistent with an outwardly propagating shock front, located $\sim 33'$ (910 kpc) from the cluster center. More recently, Churazov et al. (2021) used X-ray data from eROSITA and confirmed the presence of a shock wave in the west, with a Mach number $M \sim 1.5$. This shock is interpreted as a secondary shock, or “mini-accretion shock,” driven by the first passage of the NGC 4839 group through the cluster before reaching the apocenter and inverting its orbital motion. According to this scenario, both the relic and the west shock would be caused by the merger of NGC 4839 with the Coma Cluster. During its first passage, NGC 4839 would have driven a first shock that should now be located at the position marked by the radio relic. The gas displaced by the merger would settle back into hydrostatic equilibrium, forming a “mini-accretion” shock. We refer the reader to Burns et al. (1994), Lyskova et al. (2019), Churazov et al. (2021), and Zhang et al. (2021) for a more detailed explanation of the proposed merging scenario.

Our LOFAR image confirms the presence of an edge of the radio halo toward the west (see Figure 4), which could be in line with the scenario explained above. Shocks in the ICM are often associated with radio relics, where they leave a clear imprint on the spectral index distribution. The spectral index profile is flatter where particles are freshly re-accelerated and

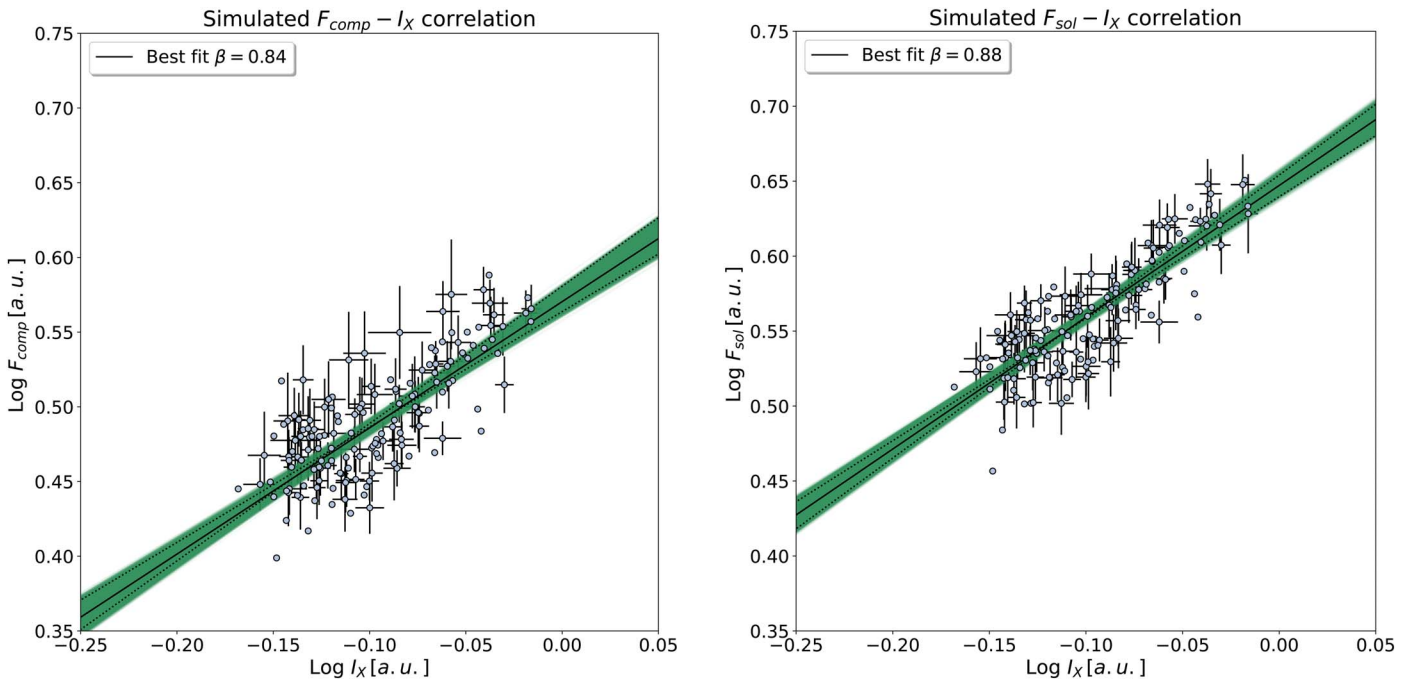


Figure 18. Left panel: $F_{\text{Comp}}-I_X$ correlation from simulated data. Right panel: $F_{\text{Sol}}-I_X$ correlation from simulated data.

Table 6

Correlation between Thermal and Non-thermal Simulated Quantities

	β	10%–90%	ρ_P
$F_{\text{Sol}}-I_X$	0.88	0.94–0.81	0.8
$F_{\text{Comp}}-I_X$	0.85	0.92–0.77	0.8
Halo Core			
$F_{\text{Sol}}-I_X$	0.5	0.6–0.4	0.2
$F_{\text{Comp}}-I_X$	0.5	0.6–0.3	0.3
Outer Halo			
$F_{\text{Sol}}-I_X$	0.83	0.91–0.75	0.8
$F_{\text{Comp}}-I_X$	0.78	0.87–0.69	0.8
$F_{\text{Sol}}-\gamma_{\text{sim}}$	1.9	2.0–1.7	0.8
$F_{\text{Comp}}-\gamma_{\text{sim}}$	1.8	1.9–1.7	0.8

Note. Column (1): quantities considered in the correlation. Column (2): best-fit slope (median value of the posterior distribution). Column (3): 10th–90th percentiles of the slope posterior distribution. Column (4): Pearson correlation coefficient.

steeper moving toward the downstream region where particles radiate their energy via synchrotron and inverse Compton losses. We have investigated whether a similar trend is found in the “halo front,” computing the spectral index profile in annuli that follow the front (Figure 20). To derive the spectral index values, we have used the same images presented in Section 5.²² In Figure 20, we show the spectral index profile obtained in annuli that follow the front, in comparison with the global spectral index trend obtained in annuli centered on the cluster and excluding the halo front region (Figure 20, left panel). We note that in the direction of the front the spectral index is flatter,

²² We recompute the spectral index radial trend in this section to better highlight the differences between the front region and the rest of the halo, while in Figure 9 we have divided the halo into four identical sectors. For the same reason, the spectral index is computed out to a smaller distance from the cluster center than in Figure 9.

but no steepening in the putative downstream region is present. However, the outermost annuli seem to follow a different trend than the global halo profile: the spectral index remains almost constant, while a radial steepening is detected when the whole halo is considered. It is possible that we are limited by the resolution, as the width of the annuli is $\sim 2'$, corresponding to ~ 60 kpc, which is larger than the electron cooling length in the post-shock region (e.g., Kang et al. 2012). Hence, it is possible that we do not have the resolution to separate the shock front from the post-shock region, where particles have already experienced strong radiative losses. An alternative scenario is that the radio front could be radio plasma re-accelerated by the same mechanism responsible for the halo emission and then dragged by the shock passage and compressed by it. Possibly, future high-resolution observations at higher or lower frequency will allow us to understand whether the halo front shows the typical shocked spectral index profile that we detect in radio relics or not.

10. The NAT–Relic Connection

The diffuse emission connecting the relic to the NAT radio galaxy NGC 4789 is imaged here with unprecedented resolution, which allows us to detect substructures in its surface brightness distribution. In particular, the bent jets of NGC 4789 do not blend smoothly into the diffuse emission, as observed in other cases of radio galaxies nearby relics (Bonafede et al. 2014; van Weeren et al. 2017; Stuardi et al. 2019), and two discontinuities between the endpoint of the jets and the diffuse emissions are detected. At the center of the diffuse source region, there is a bright transverse bar. Such a bar has been detected in other bent tails (e.g., in A2443, Clarke et al. 2013; and recently in the Shapley supercluster, Venturi et al. 2022) and is predicted by simulations of interacting AGN tails and shocks (Nolting et al. 2019). The length of this source, measured from the relic’s edge down to the endpoints of the jets, is $10'$, corresponding to 280 kpc at the Coma redshift.

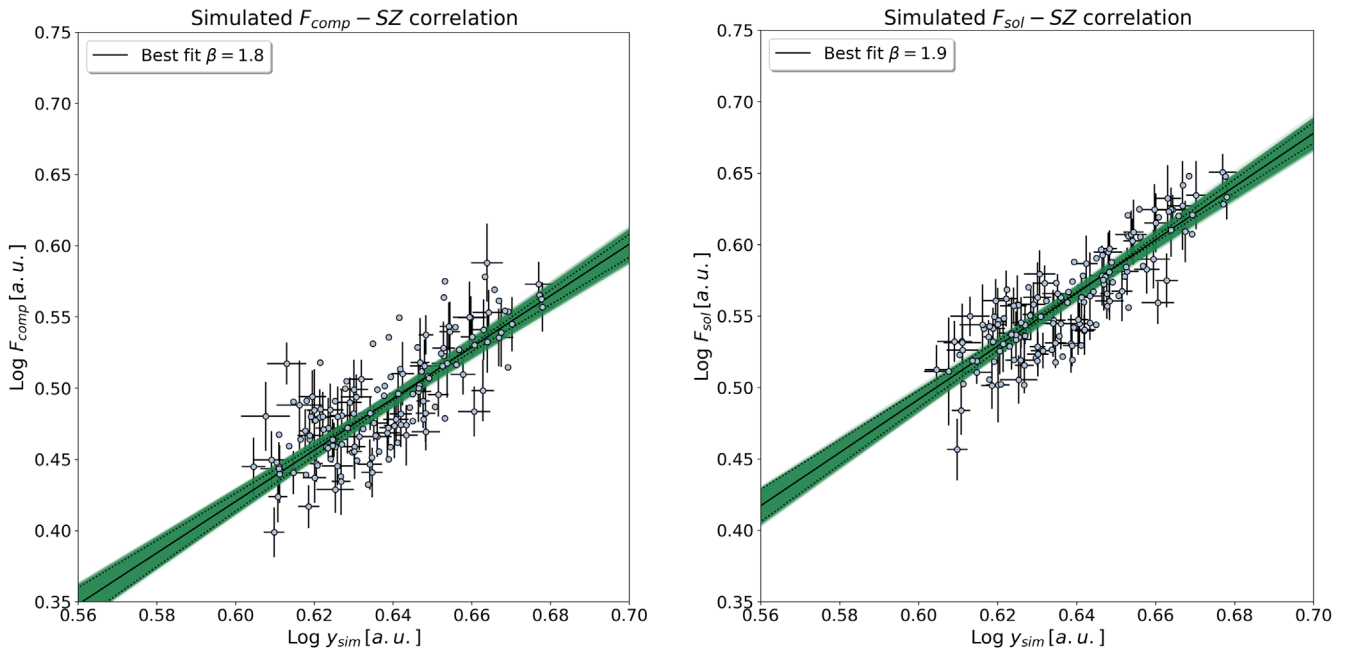


Figure 19. Left panel: $F_{\text{Comp}} - \text{SZ}$ correlation from simulated data. Right panel: $F_{\text{Sol}} - \text{SZ}$ correlation from simulated data.

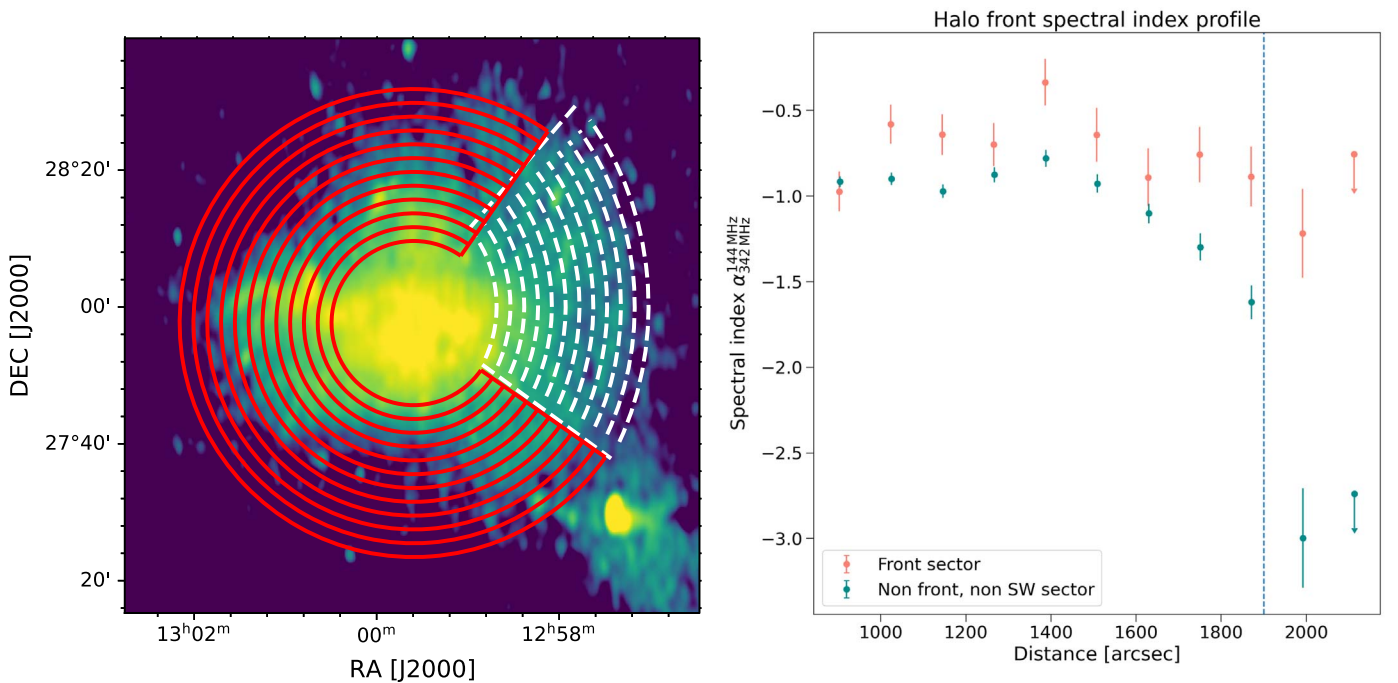


Figure 20. Left panel: annuli used to compute the spectral index trend in the halo front region (white dashed) and in the outer halo (red). Right: spectral index trend computed in the annuli shown in the left panel. Arrows indicate 3σ upper limits. The vertical dashed line indicates the position of the halo front. Error bars only show statistical errors; the values of the spectral index are also affected by the flux calibration uncertainties of WSRT and LOFAR (10% and 15%, respectively), which would contribute with an additional error of 0.2.

To investigate the possible connection of the radio plasma with the thermal gas, we have used the ROSAT image and the radio image at $35''$ resolution and investigated the existence of a correlation between the thermal and non-thermal plasma, as done already for the radio halo (see Section 6) and for the Coma bridge (Bonafede et al. 2021).

The average brightness profile of the NAT–relic connection is largely constant, increasing close to the relic edge, where the radio bar is located. In addition, the low counts in the X-ray

image do not allow us to make a proper analysis. Hence, though no correlation or anticorrelation between the two quantities seems to be present, no firm conclusions can be derived, and we cannot rule out that the radio emission originates from phenomena similar to those responsible for the bridge. However, given its morphology, we will investigate below an alternative scenario.

The spectral index trend along the NAT–relic connection main axis is shown in Figure 21. We have used the WSRT R

image (see Table 2 in Giovannini et al. 1991) that has been used already in Bonafede et al. (2021) to analyze the bridge. Although the higher resolution of the image by Brown & Rudnick (2011) would provide a better description of the spectral index trend, calibration errors from Coma A are strongly affecting that region. The spectrum of the radio emission computed between 144 and 326 MHz shows a gradual steepening from regions close to the AGN core toward the relic’s outer edge, reaching values of $\alpha = -1.6 \pm 0.2$. At the relic’s outer edge, the spectral index flattens to $\alpha = -1.2 \pm 0.2$, and it steepens toward the NE, i.e., the putative post-shock region, reaching again $\alpha = -1.6 \pm 0.2$. We note that the spectrum starts to flatten already in front of the relic edge (at $\sim 77'$ from the cluster center), though within the error that value is consistent with the steepest point. This apparent flattening could be due to projection effects, as if the relic has a velocity component along the line of sight, some relic emission could appear in front of the relic edge in projection.

Overall, the spectral trend detected along the tail of NCG4789 and in the NAT–relic connection is consistent with AGN particle aging. NGC 4789 would be moving toward the SW of the cluster injecting particles into the ICM. Thus, more recently injected particles are closer to the AGN core than the older ones that have been left behind. The shape of the source and the connection with the radio relic make this source peculiar and suggest a link between the NAT–relic connection and the shock wave that would power the radio relic.

However, according to the merging scenario outlined in several papers (Venturi et al. 1990; Giovannini et al. 1991; Churazov et al. 2021), NGC 4789 would be in the pre-shock region. Hence, it is puzzling to understand how features like the bar could have been formed because that emission has not yet interacted with the shock. Enßlin & Gopal-Krishna (2001) have proposed that the plasma from NGC 4789 is dragged by the infalling matter (falling into Coma’s cluster) to the location of the relic, where it is re-energised adiabatically by the shock wave.

Three possible scenarios could in principle explain the emission of the NAT and its connection with the relic, and we briefly outline them here:

1. NGC 4789 is in the pre-shock region, and the shock wave responsible for the relic is moving toward the SW and approaching the tail. In this scenario, the emission from the tail in the NAT–relic connection region would be unaffected by the shock passage. However, the plasma injected into the ICM by the tail would play an important role in explaining the relic emission, as it would furnish energetic electrons that the low Mach number shock wave would reaccelerate.
2. The relic is powered by a quasi-stationary accretion shock, and NGC 4789 is moving supersonically and crossing the shock region from NE to SW. Hence, NGC 4789 would be in the pre-shock region, but its tail would have crossed the shock wave responsible for the relic emission.
3. The relic is powered by a shock wave that is moving toward the cluster center. NGC 4789 has been crossed by the shock, and it is now in the post-shock region.

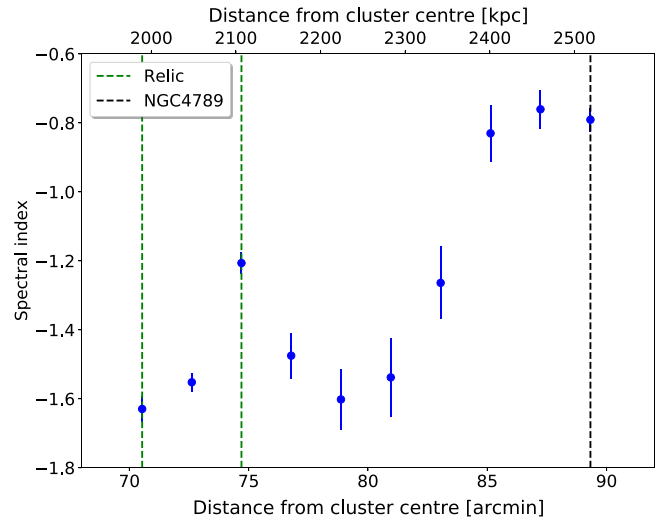


Figure 21. Spectral index profile between 326 and 144 MHz of the emission called the NAT–relic connection. Images at the WSRT resolution ($100'' \times 150''$) have been used to compute the spectral index in each box.

Scenario (iii) has been recently studied by Nolting et al. (2019) using numerical simulations. They have analyzed the case of a shock wave that crosses an AGN when the shock normal is perpendicular to the jets. They find that when a shock passes through the active jets and lobes of an AGN, jets are distorted by the shock passage, creating an NAT morphology, and a structure similar to the radio bar, as observed here. The spectral index trend resulting from the simulations by Nolting et al. (2019) is in agreement with the one observed here along the tail and NAT–relic connection, though the values are slightly flatter after 200 Myr from the shock passage, when the simulation stops. This scenario would require a shock wave moving toward the cluster center, which seems disfavored by some authors (Feretti et al. 2005; Akamatsu et al. 2013; Churazov et al. 2021) and also by the spectral index trend across the relic that we detect, which is steepening NE, in agreement with expectation from an outward-moving shock wave. In scenario (ii), the situation would have some similarities with the simulation by Nolting et al. (2019), as also in this scenario the AGN would be crossed by a shock. However, in this case, the AGN would be in the pre-shock region, and its tail would be interacting with a less dense environment than the one simulated by Nolting et al. (2019). Scenario (ii) seems also supported by the analysis of Adami et al. (2005), where they detect a relative velocity of $\sim 1000 \text{ km s}^{-1}$ between NGC 4789 and NGC 4839, at the cluster center. Our analysis does not allow us to discard scenario (i), where the shock is overtaking the preexisting tail from the back. We can see that the tail and shock must be interacting because the tail abruptly stops at the position of the relic. This situation has not been simulated yet, but it is likely that it would require some fine-tuning of the parameters. We indicate scenario (ii) as the favored one, given the data we have now, though it remains to be seen whether the interaction of the AGN tail with a preshocked environment at the cluster outskirts would create the substructures that we observe. In all scenarios, the NAT galaxy NGC 4789 would be providing seed electrons that are (re)accelerated by the shock and originate the radio relic. In the literature, there are a few other cases where a link between an AGN tail and a relic has been established (see Bonafede et al. 2014; van Weeren et al. 2017; Stuardi et al. 2019).

11. Discussion and Conclusions

In this work, we have used new data at 144 MHz from LOFAR to analyze the emission from the Coma cluster. We summarize our findings in the following and discuss how these observations allow us to advance our understanding of the non-thermal emission in clusters of galaxies.

We have focused our analysis on the properties of the radio halo, which—detected at 144 MHz with the resolution and sensitivity allowed by LOFAR—presents new interesting features and allows us to perform detailed resolved studies of the radio emission. We find the following:

1. The radio halo at 144 MHz appears larger than previously reported in the literature, with a largest angular scale of $\sim 71'$, corresponding to ~ 2 Mpc. The halo is connected to the relic through a low surface brightness radio bridge, and the relic is connected to the AGN NGC 4879 to the SW. In total, the radio emission from the halo to the head of NGC 4879 spans $\sim 2^\circ$, corresponding to ~ 3.4 Mpc.
2. The halo brightness profile is well fitted by an exponential elliptical profile. At 144 MHz, it is characterized by e -folding radii $r_1 = 355$ kpc and $r_2 = 268$ kpc. At 325 MHz, the profile is more peaked, with $r_1 = 268$ kpc and $r_2 = 240$ kpc. This is consistent with a spectral steepening of the radio emission toward the halo outskirts, in agreement with the results by Giovannini et al. (1993). It would be useful to perform these fits also at other frequencies in order to study how the halo size changes with frequency.
3. The spectrum of the radio halo between 144 and 342 MHz is flatter than previously reported, though consistent within the errors. We find $\alpha = -1.0 \pm 0.2$, while previous studies indicate $\alpha \sim -1.2$. We have computed the flux density of the halo at both frequencies from the best-fit exponential model, which is less affected by the different sensitivities of the two images and the possible presence of residuals from unrelated sources.
4. We have computed the radial trend of the spectral index α dividing the halo into four symmetric sectors. Our estimates could still be affected by residual contamination from unrelated source and calibration errors, but these should not have a major impact on the global results. We detect for the first time a moderate steepening toward the cluster center of the spectral index and confirm the steepening toward the cluster outskirts found at higher frequencies by Giovannini et al. (1993). This trend is in agreement with the expectations of homogeneous turbulent re-acceleration models. Though a detailed modeling is needed to understand the effect of projection effects and the exact location of the steepening frequency, we argue that the steepening detected at the cluster outskirts could indicate a non-constant acceleration time and hint at a constant turbulent Mach number. The spectral index steepening toward the cluster center is more or less pronounced in the different sectors, being prominent in the SW sector and not clearly detected in the NE sector. It is possible that the SW sector has been perturbed by the passage of the NGC 4839 group and shows now different properties.
5. The point-to-point analysis between radio and X-ray surface brightness indicates a sublinear slope of non-thermal plasma with respect to the thermal plasma. We

obtain $I_R \propto I_X^{0.64}$ when the correlation is computed on images at $1'$ resolution. We detect a steeper, yet sublinear, correlation when the radio image is convolved with Gaussian kernels of $2'$, $3'$, $4'$, $5'$, and $6'$, and it converges to $I_R \propto I_X^{0.76}$. Indeed, images at lower resolution are more sensitive to the weak emission in the halo outermost regions. We note that the total halo flux density does not change when computed from the $35''$ or $6'$ image because the outermost regions of the halo yield a very minor contribution to the total halo flux density. However, these regions affect the radio–X-ray correlation, making it steeper.

6. We have investigated whether the radio–X-ray correlation has a different slope in the halo core than in the outer halo, finding that the correlation is flatter in the core ($I_R \propto I_X^{0.41}$) than in the outer halo ($I_R \propto I_X^{0.76}$). By investigating the radial trend of the quantity I_R-I_X , we have confirmed that this trend can be interpreted as a radial trend of I_R versus I_X being flatter in the halo core. An opposite slope change has been recently found in some cool-core clusters, where the mini halo emission is surrounded by a weaker and more extended component (Biava et al. 2021). A flatter slope in the halo core is inconsistent with a major contribution of secondary electrons produced through hadronic interaction between thermal protons and cosmic-ray protons in the ICM.
7. In the framework of homogeneous re-acceleration models, the change of the slope of the I_R-I_X correlation can be only partially accounted for by a declining magnetic field profile. We have investigated the role of X , i.e., the ratio of CRE to thermal energy density, and find that a radially increasing value of X would provide a better match with data. Although more detailed modeling should be done to derive firm conclusions, we note that an increasing value of X with the distance from the cluster center is also expected from a theoretical point of view.
8. With the help of MHD cosmological simulations, we have computed the turbulent energy flux associated with the compressive and solenoidal velocity components in a Coma-like cluster, and we find that both quantities show a sublinear scaling with the simulated X-ray emission, which is in agreement with the observed scaling of I_R versus I_X . Assuming the same efficiency for both modes, the flux associated with the solenoidal velocity component is a factor 10 higher than the flux associated with the compressive component. Hence, once the CRE distribution throughout the volume is assumed, it would be possible to constrain the relative importance of the two modes in the process of particle acceleration.

From the analysis of the Coma field, we also conclude the following:

1. To the NE of Coma, at a projected distance of $\sim 1.2 R_{\text{vir}}$, an arc-like diffuse patch of emission is discovered. As a large-scale filament of galaxies is detected in that direction, we tentatively propose that this emission is due to particles re-accelerated by an accretion shock, and we name this emission “accretion relic.” If confirmed, this would be the first detection of particle acceleration from an accretion shock.
2. The halo front, already reported by Brown & Rudnick (2011), is here confirmed coincident with the position of

a shock front detected in both X-ray and SZ studies (Planck Collaboration et al. 2013; Churazov et al. 2021). The radio spectral index does not seem to follow the typical trend found in radio relics. However, the large errors due to the small frequency range used to compute the spectral index do not allow us to exclude such a trend. It is possible that the halo front is caused by the radio halo plasma dragged along by the shock wave and compressed by it. In any case, we can conclude that the properties of the halo in the west region are affected by the shock passage.

3. The radio relic in the Coma cluster is here imaged with unprecedented detail, thanks to both the sensitivity of the LOFAR observations and the calibration techniques that we have used, which allow us to minimize the artifacts from Coma A. The relic emission is connected to the tail of NGC 4879, which is likely moving toward the SW. The connection between the relic and NGC 4879 is what we name the NAT–relic connection. The 20'' resolution image shows that the endpoints of the NGC 4879 jets are well distinct from the weak diffuse emission of the NAT–relic connection. A bright bar of radio emission is detected, similar to what has been found in other cluster tails (e.g., Clarke et al. 2013). We have discussed three possible scenarios to explain the presence of the NAT–relic connection and propose that NGC 4879 is moving supersonically toward the SW. During its motion, it has crossed the shock at the position of the relic. The shock has reenergized the particles injected by the tail in the ICM in the past and left behind during the galaxy’s motion through the ICM.

Using literature information about the merging scenario of Coma and its large-scale structure environment, we can outline a global picture to explain the observed radio emission. The Coma cluster is currently accreting matter through filaments of galaxies that connect it to A1367 (Malavasi et al. 2020). A recent merger has happened between Coma and the galaxy group NGC 4839, which has passed the cluster from NE to SW, injecting a first shock wave in the ICM that is now powering the radio relic emission (Lyskova et al. 2019). The cluster core has been perturbed by this merger, and possibly from previous less massive mergers, which have released thermal energy in the ICM. A small fraction of this energy has been dissipated in turbulent motions, which have re-accelerated a mildly relativistic population of CRE already present in the ICM originating the radio halo.

From the global spectral index of the halo, its radial trend, and the analysis of the radio–X-ray correlation, we are able to derive a coherent picture where particles are re-accelerated by homogeneous turbulence in the ICM. In this picture, we have made several working assumptions that indicate possible regimes for re-acceleration to operate (i.e., constant turbulent Mach number and a radial increase of the CRE energy density with respect to the thermal energy density). We have attempted to distinguish between re-acceleration by Transit-Time-Damping with compressive modes and non-resonant second-order Fermi acceleration with solenoidal modes, and although present data are not accurate enough, we have shown that observations are entering a regime where the details of the model can be in principle tested. It is possible that future observations, either with LOFAR 2.0 and/or MeerKAT, will be able to make an

additional step forward and unveil the details of turbulent re-acceleration.

The cluster core has been perturbed by the passage of NGC 4839, and its motion around its equilibrium position has caused a second shock wave (Lyskova et al. 2019; Churazov et al. 2021) whose front is now coincident with the halo front. We find that the spectrum of the halo front has been affected by the shock passage, but we are not able to distinguish between shock re-acceleration or compression by the shock wave.

NGC 4839 is now at its second passage toward the cluster center (Lyskova et al. 2019; Churazov et al. 2021). Its motion might have injected additional turbulence in the ICM and a considerable amount of seed electrons, which originate the radio bridge (Bonafede et al. 2021). The NAT galaxy NGC 4789 that is now located to the SW of the relic is moving away from the cluster center at a supersonic velocity after crossing the shock wave at the location of the relic. From this interaction, the radio plasma injected in the ICM by NGC 4789 has been reenergized, leading to the emission that we detect in the NAT–relic connection.

Finally, a filament of matter is detected to the NE of the Coma cluster. The matter accreting toward the cluster from that direction could result in the tentative “accretion relic” that we have discovered.

The scenario that we outline here is not the only possible one, and it leaves open questions. However, our analysis shows that we are entering a new era for the physics of non-thermal ICM emission, where we can constrain the model parameters.

A.B., E.B., N.B., and C.J.R. acknowledge support from the ERC Starting Grant “DRANOEL,” No. 714245. A.B. and C.S. acknowledge support from the MIUR grant FARE “SMS.” F.V., K.R., and M. Brienza acknowledge support from the ERC Starting Grant “MAGCOW,” No. 714196. H.B. and P.M. acknowledge financial contribution from the contracts ASI-INAF Athena 2019-27-HH.0, “Attività di Studio per la comunità scientifica di Astrofisica delle Alte Energie e Fisica Astroparticellare” (Accordo Attuativo ASI-INAF n. 2017-14-H.0), from the European Union’s Horizon 2020 Programme under the AHEAD2020 project (grant agreement No. 871158), and support from INFN through the InDark initiative. M. Brüggemack acknowledges funding by the Deutsche Forschungsgemeinschaft (DFG, German Research Foundation) under Germany’s Excellence Strategy EXC 2121 Quantum Universe 390833306. A. Botteon acknowledges support from the VIDI research program with project No. 639.042.729, which is financed by the Netherlands Organisation for Scientific Research (NWO). R.J.v.W. acknowledges support from the ERC Starting Grant ClusterWeb 804208. X.Z. acknowledges support from Chinese Scholarship Council (CSC). A.S. is supported by the Women In Science Excel (WISE) program of the NWO. M.R. and F.G. acknowledge support from INAF mainstream project “Galaxy Clusters science with LOFAR.” LOFAR, the Low Frequency Array designed and constructed by ASTRON, has facilities owned by various parties (each with their own funding sources) and that are collectively operated by the International LOFAR Telescope (ILT) foundation under a joint scientific policy. The LOFAR software and dedicated reduction packages on https://github.com/apmechev/GRID_LRT were deployed on the e-infrastructure by the LOFAR e-infragroup, consisting of J.B.R.O. (ASTRON & Leiden Observatory), A.P.M. (Leiden Observatory), and T.S. (Leiden





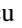







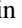

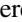
Observatory) with support from N. Danezi (SURFsara) and C. Schrijvers (SURFsara). This research had made use of the NASA/IPAC Extragalactic Database (NED), which is operated by the Jet Propulsion Laboratory, California Institute of Technology, under contract with the National Aeronautics and Space Administration.

Software: Ciao v4.13 (Fruscione et al. 2006), ENZO (Bryan et al. 2014; Vazza et al. 2018), Astropy (Astropy Collaboration et al. 2013, 2018) DDFacet (Tasse et al. 2018) APLpy (Robitaille & Bressert 2012), wsclean (Offringa & Smirnov 2017).

Appendix XMM-Newton ObsIDs

The ObsIDs of the XMM-Newton observations we analyzed are 58940701, 124710101, 124710301, 124710401, 124710501, 124710601, 124710701, 124710801, 124710901, 124711101, 124711401, 124711601, 124712001, 124712101, 124712201, 124712401, 124712501, 153750101, 204040101, 204040201, 204040301, 300530101, 300530201, 300530301, 300530401, 300530501, 300530601, 300530701, 304320201, 304320301, 304320801, 403150101, 403150201, 403150301, 403150401, 652310201, 652310301, 652310401, 652310501, 652310601, 652310701, 652310801, 652310901, 652311001, 691610201, 691610301, 800580101, 800580201, 851180501, 841680101, 841680201, 841680401, 841680501, 841680301, 841680801, 841680601, and 841680701.

ORCID iDs

A. Bonafede  <https://orcid.org/0000-0002-5068-4581>
 L. Rudnick  <https://orcid.org/0000-0001-5636-7213>
 G. Giovannini  <https://orcid.org/0000-0003-4916-6362>
 T. W. Shimwell  <https://orcid.org/0000-0001-5648-9069>
 A. Simionescu  <https://orcid.org/0000-0002-9714-3862>
 M. Brüggen  <https://orcid.org/0000-0002-3369-7735>
 K. Rajpurohit  <https://orcid.org/0000-0001-7509-2972>
 C. Stuardi  <https://orcid.org/0000-0003-1619-3479>
 L. Feretti  <https://orcid.org/0000-0003-0312-6285>
 A. Botteon  <https://orcid.org/0000-0002-9325-1567>
 E. Carretti  <https://orcid.org/0000-0002-3973-8403>
 R. Cassano  <https://orcid.org/0000-0003-4046-0637>
 F. de Gasperin  <https://orcid.org/0000-0003-4439-2627>
 F. Gastaldello  <https://orcid.org/0000-0002-9112-0184>
 R. J. van Weeren  <https://orcid.org/0000-0002-0587-1660>

References

Adami, C., Biviano, A., Durret, F., & Mazure, A. 2005, *A&A*, 443, 17
 Akamatsu, H., Inoue, S., Sato, T., et al. 2013, *PASJ*, 65, 89
 Astropy Collaboration, Price-Whelan, A. M., Sipőcz, B. M., et al. 2018, *AJ*, 156, 123
 Astropy Collaboration, Robitaille, T. P., Tollerud, J., et al. 2013, *A&A*, 558, A33
 Baldi, A. S., Bourdin, H., Mazzotta, P., et al. 2019, *A&A*, 630, A121
 Ballarati, B., Feretti, L., Ficarra, A., et al. 1981, *A&A*, 100, 323
 Biava, N., de Gasperin, F., Bonafede, A., et al. 2021, *MNRAS*, 508, 3995
 Bonafede, A., Brunetti, G., Vazza, F., et al. 2021, *ApJ*, 907, 32
 Bonafede, A., Feretti, L., Murgia, M., et al. 2010, *A&A*, 513, A30
 Bonafede, A., Intema, H. T., Brüggen, M., et al. 2014, *MNRAS*, 444, L44
 Bonafede, A., Vazza, F., Brüggen, M., et al. 2013, *MNRAS*, 433, 3208
 Botteon, A., Brunetti, G., van Weeren, R. J., et al. 2020a, *ApJ*, 897, 93
 Botteon, A., van Weeren, R. J., Brunetti, G., et al. 2020b, *MNRAS*, 499, L11
 Boxelaar, J., van Weeren, R., & Botteon, A. 2021, *A&C*, 35, 100464
 Botteon, A., Shimwell, T. W., Cassano, R., et al. 2022, *A&A*, 660, A78
 Briel, U. G., Henry, J. P., Lumb, D. H., et al. 2001, *A&A*, 365, L60

Brown, S., & Rudnick, L. 2011, *MNRAS*, 412, 2
 Brunetti, G., Giacintucci, S., Cassano, R., et al. 2008, *Natur*, 455, 944
 Brunetti, G., & Jones, T. W. 2014, *IMPD*, 23, 1430007
 Brunetti, G., & Lazarian, A. 2007, *MNRAS*, 378, 245
 Brunetti, G., & Lazarian, A. 2011, *MNRAS*, 410, 127
 Brunetti, G., & Lazarian, A. 2016, *MNRAS*, 458, 2584
 Brunetti, G., Rudnick, L., Cassano, R., et al. 2013, *A&A*, 558, A52
 Brunetti, G., Setti, G., Feretti, L., & Giovannini, G. 2001, *MNRAS*, 320, 365
 Brunetti, G., & Vazza, F. 2020, *PhRvL*, 124, 051101
 Bryan, G. L., Norman, M. L., O'Shea, B. W., et al. 2014, *ApJS*, 211, 19
 Burns, J. O., Roettiger, K., Ledlow, M., & Klypin, A. 1994, *ApJL*, 427, L87
 Cassano, R., & Brunetti, G. 2005, *MNRAS*, 357, 1313
 Churazov, E., Khabibullin, I., Lyskova, N., Sunyaev, R., & Bykov, A. M. 2021, *A&A*, 651, A41
 Clarke, T. E., Randall, S. W., Sarazin, C. L., Blanton, E. L., & Giacintucci, S. 2013, *ApJ*, 772, 84
 Condon, J. J., Cotton, W. D., Greisen, E. W., et al. 1998, *AJ*, 115, 1693
 Cordey, R. A. 1985, *MNRAS*, 215, 437
 Cuciti, V., Cassano, R., Brunetti, G., et al. 2015, *A&A*, 580, A97
 Donert, J., Dolag, K., Lesch, H., & Müller, E. 2009, *MNRAS*, 392, 1008
 Enßlin, T. A., & Gopal-Krishna 2001, *A&A*, 366, 26
 Feretti, L., Schuecker, P., Böhringer, H., Govoni, F., & Giovannini, G. 2005, *A&A*, 444, 157
 Fruscione, A., McDowell, J. C., Allen, G. E., et al. 2006, *Proc. SPIE*, 6270, 62701V
 Gastaldello, F., Ghizzardi, S., Marelli, M., et al. 2017, *ExA*, 44, 321
 Giovannini, G., Feretti, L., & Stanghellini, C. 1991, *A&A*, 252, 528
 Giovannini, G., Feretti, L., Venturi, T., Kim, K.-T., & Kronberg, P. P. 1993, *ApJ*, 406, 399
 Govoni, F., Feretti, L., Giovannini, G., et al. 2001, *A&A*, 376, 803
 Govoni, F., Orrù, E., Bonafede, A., et al. 2019, *Sci*, 364, 981
 Hanisch, R. J., & Erickson, W. C. 1980, *AJ*, 85, 183
 Hardcastle, M. J., Gürkan, G., van Weeren, R. J., et al. 2016, *MNRAS*, 462, 1910
 Hoang, D. N., Brüggen, M., & Botteon, A. 2022, arXiv:2206.04666
 Hoang, D. N., Zhang, X., Stuardi, C., et al. 2021, *A&A*, 656, A154
 Hong, S. E., Ryu, D., Kang, H., & Cen, R. 2014, *ApJ*, 785, 133
 Ignesti, A., Brunetti, G., Gitti, M., & Giacintucci, S. 2020, *A&A*, 640, A37
 Kang, H., Ryu, D., & Jones, T. W. 2012, *ApJ*, 756, 97
 Kelly, B. C. 2007, *ApJ*, 665, 1489
 Kronberg, P. P., Kothes, R., Salter, C. J., & Perillat, P. 2007, *ApJ*, 659, 267
 Large, M. I., Mathewson, D. S., & Haslam, C. G. T. 1959, *Natur*, 183, 1663
 Lyskova, N., Churazov, E., Zhang, C., et al. 2019, *MNRAS*, 485, 2922
 Malavasi, N., Aghanim, N., Tanimura, H., Bonjean, V., & Douspis, M. 2020, *A&A*, 634, A30
 Marelli, M., Molendi, S., Rossetti, M., et al. 2021, *ApJ*, 908, 37
 Markevitch, M. 2010, arXiv:1010.3660
 Miniati, F., & Beresnyak, A. 2015, *Natur*, 523, 59
 Mirakhor, M. S., & Walker, S. A. 2020, *MNRAS*, 497, 3204
 Murgia, M., Govoni, F., Markevitch, M., et al. 2009, *A&A*, 499, 679
 Nolting, C., Jones, T. W., O'Neill, B. J., & Mendygral, P. J. 2019, *ApJ*, 885, 80
 Offringa, A. R., & Smirnov, O. 2017, *MNRAS*, 471, 301
 Ogrea, G. A., & Brüggen, M. 2013, *MNRAS*, 433, 1701
 Ogrea, G. A., Brüggen, M., van Weeren, R. J., et al. 2013, *MNRAS*, 433, 812
 Pfrommer, C., & Enßlin, T. A. 2004, *A&A*, 413, 17
 Pizzo, R. F. 2010, PhD Thesis, Kapteyn Institute
 Planck Collaboration, Abergel, A., Ade, P. A. R., et al. 2014, *A&A*, 571, A11
 Planck Collaboration, Ade, P. A. R., Aghanim, N., et al. 2011, *A&A*, 536, A8
 Planck Collaboration, Ade, P. A. R., Aghanim, N., et al. 2013, *A&A*, 554, A140
 Planck Collaboration, Akrami, Y., Ashdown, M., et al. 2020, *A&A*, 644, A99
 Raja, R., Rahaman, M., Datta, A., et al. 2020, *MNRAS*, 493, L28
 Rajpurohit, K., Brunetti, G., Bonafede, A., et al. 2021a, *A&A*, 646, A135
 Rajpurohit, K., Hoefl, M., Vazza, F., et al. 2020, *A&A*, 636, A30
 Rajpurohit, K., van Weeren, R. J., Hoefl, M., et al. 2022, *ApJ*, 927, 80
 Rajpurohit, K., Vazza, F., van Weeren, R. J., et al. 2021b, *A&A*, 654, A41
 Riseley, C. J., Rajpurohit, K., Loi, F., et al. 2022, *MNRAS*, 512, 4210
 Robitaille, T., & Bressert, E. 2012, APLpy: Astronomical Plotting Library in Python, Astrophysics Source Code Library, ascl:1208.017
 Rudnick, L. 2002, *NewAR*, 46, 101
 Savini, F., Bonafede, A., Brüggen, M., et al. 2018, *MNRAS*, 478, 2234
 Savini, F., Bonafede, A., Brüggen, M., et al. 2019, *A&A*, 622, A24
 Shimwell, T. W., Hardcastle, M. J., Tasse, C., et al. 2022, *A&A*, 659, A1
 Shimwell, T. W., Röttgering, H. J. A., Best, P. N., et al. 2017, *A&A*, 598, A104
 Shimwell, T. W., Tasse, C., Hardcastle, M. J., et al. 2019, *A&A*, 622, A1

- Simionescu, A., Werner, N., Urban, O., et al. 2013, *ApJ*, 775, 4
- Stuardi, C., Bonafede, A., Wittor, D., et al. 2019, *MNRAS*, 489, 3905
- Tasse, C., Hugo, B., Mirmont, M., et al. 2018, *A&A*, 611, A87
- Thierbach, M., Klein, U., & Wielebinski, R. 2003, *A&A*, 397, 53
- Trasatti, M., Akamatsu, H., Lovisari, L., et al. 2015, *A&A*, 575, A45
- van Haarlem, M. P., Wise, M. W., Gunst, A. W., et al. 2013, *A&A*, 556, A2
- van Weeren, R. J., Andrade-Santos, F., Dawson, W. A., et al. 2017, *NatAs*, 1, 0005
- van Weeren, R. J., de Gasperin, F., Akamatsu, H., et al. 2019, *SSRv*, 215, 16
- van Weeren, R. J., Röttgering, H. J. A., Rafferty, D. A., et al. 2012, *A&A*, 543, A43
- Vazza, F., Brunetti, G., Brüggén, M., & Bonafede, A. 2018, *MNRAS*, 474, 1672
- Vazza, F., Jones, T. W., Brüggén, M., et al. 2017, *MNRAS*, 464, 210
- Vazza, F., Locatelli, N., Rajpurohit, K., et al. 2021, *Galax*, 9, 109
- Venturi, T., Giacintucci, S., Merluzzi, P., et al. 2022, *A&A*, 660, A81
- Venturi, T., Giovannini, G., & Feretti, L. 1990, *AJ*, 99, 1381
- Venturi, T., Rossetti, M., Brunetti, G., et al. 2017, *A&A*, 603, A125
- Wilber, A., Brüggén, M., Bonafede, A., et al. 2018, *MNRAS*, 473, 3536
- Zhang, C., Churazov, E., & Zhuravleva, I. 2021, *MNRAS*, 501, 1038
- Zhang, X., Simionescu, A., Akamatsu, H., et al. 2020, *A&A*, 642, A89
- ZuHone, J. A., Markevitch, M., Brunetti, G., & Giacintucci, S. 2013, *ApJ*, 762, 78